

This is the author-created version of the following work:

Xiao, Yuan, and Lin, Wenxian (2022) *Linear temporal stability analysis on cross sheared flow: the stabilization effects via cross shear*. *Physics of Fluids*, 34 .

Access to this file is available from:

<https://researchonline.jcu.edu.au/72699/>

© 2022 Author(s). This article may be downloaded for personal use only. Any other use requires prior permission of the author and AIP Publishing. This article appeared in *Phys. Fluids* 34, 034101 (2022); <https://doi.org/10.1063/5.0083687> and may be found at <https://aip.scitation.org/doi/abs/10.1063/5.0083687>.

Please refer to the original source for the final version of this work:

<https://doi.org/10.1063/5.0083687>

This is the author's peer reviewed, accepted manuscript. However, the online version of record will be different from this version once it has been copyedited and typeset.

PLEASE CITE THIS ARTICLE AS DOI: 10.1063/5.0083687

Linear temporal stability analysis on cross sheared flow: the stabilization effects via cross shear

Yuan Xiao (肖原)^{1,2} and Wenxian Lin (林文宪)^{2, a)}

¹⁾*School of Mechatronic & Vehicle Engineering, East China Jiaotong University, Nanchang, Jiangxi 330013, China*

²⁾*College of Science & Engineering, James Cook University, Townsville, QLD 4811, Australia*

(Dated: 3 February 2022)

The stability features of the inviscid, homogenous and free cross sheared flow, with base flow velocities $U = \tanh(z)$ in the primary direction which is unstable and $V = \xi z^3$ in the orthogonal direction which is stable, are thoroughly examined with linear temporal stability analysis, where z is the transverse coordinate perpendicular to the flow and ξ is the cross shear ratio which is the ratio of the characteristic magnitudes of V to U . The map of the unstable regions directly related to $\chi = \xi(\beta/\alpha)$ is obtained, where (β/α) is the ratio between the orthogonal and primary wavenumbers. Further examination of the eigenfunctions shows that the eigenfunction structures divide into the orthogonal wavenumber (OW) mode where (β/α) dominates and the cross shear (CS) mode where ξ dominates. The cross shear is found necessary for stabilization, in spite of different fashions for the OW and CS modes. The transition from the OW mode to the CS mode shows that the developments of the two modes inherently compete with each other, so that when $\psi = (\beta/\alpha)/\xi$ decreases the enhanced cross shear needs to deteriorate the OW mode before it helps the growth of the CS mode. Based on the magnitudes of the associated eigenfunctions in the enstrophy budget, the map of the OW, CS and hybrid modes which includes the mixed features of both the OW and CS modes, is produced and discussed.

^{a)}Electronic mail: wenxian.lin@jcu.edu.au.

I. INTRODUCTION

Although the parallel sheared flow approximation, in which two-dimensional perturbations aligned with the base flow direction, for simplicity, was widely applied in hydrodynamics in the past decades, but in reality the non-parallelism of the sheared flows predominates in engineering and environmental circumstances. In contrast to the parallel approximation, the non-parallel effect in general can be considered as the misalignment between the base flow velocity (shear) and perturbations (wavenumber), accordingly it can be invoked in two ways. First, the non-parallelism can be achieved by either active or passive modifications of the streamwise/spanwise perturbations. For instance, to reduce the friction drag of the boundary flow by delaying the laminar-turbulent transition, one effective methodology is the compliant walls¹⁻⁵, in which the streamwise/spanwise perturbations are manipulated by different design fashions, *e.g.*, surface coating^{6,7}, wall-deformation⁸, and wall motion^{5,9}. Similar concepts of surface geometrical modifications are also broadly employed in other convectional flow controls, *e.g.*, splitter plate¹⁰, groove¹¹⁻¹⁴, small rotating cylinder¹⁵ and oscillated cylinder¹⁶, surface stripes and waviness¹⁷⁻¹⁹, as well as chevrons²⁰, in that three-dimensional forcing, which in essence belongs to non-parallelism, is confirmed to be more effective than two-dimensional one^{17,21}. Second, the non-parallelism can also be caused by the misalignment of the base flow, which usually involves remarkably interactive and twisted coherent structures. For the jet in cross flow (JICF) in gas turbines and propulsion systems, where a perpendicular jet flow is injected into the boundary layer flow, multiple coherent structures, *e.g.*, the counter-rotating vortex in the jet cross section, the horseshoe vortices at the leading edge of the jet and the Kelvin-Helmholtz instability^{22,23}, always interact with each other and therefore lead to even more complicated streak structures in the downstream wake region. It is also found that the overall status of the vortex structures of the JICF system depends on the velocity ratio between the cross jet flow and the boundary layer flow. Likewise, in geophysical/stratified flows, the non-parallel effects can also be induced by the flow twists, in which the flow direction and magnitudes may vary differently with height. The coherent eddy structures in the spanwise direction are experimentally²⁴ and numerically²⁵ confirmed, with, noticeably, significantly enhanced turbulent mixing. There are many examples of the non-parallelism in engineering and nature scenarios, but they are not reviewed here as it is not the focus of this paper.

This is the author's peer reviewed, accepted manuscript. However, the online version of record will be different from this version once it has been copyedited and typeset.

PLEASE CITE THIS ARTICLE AS DOI: 10.1063/1.50083687

In destabilization of a non-parallel flow, the misaligned base flow and the resultant twisted shear usually play as a governing parameter to determine the occurrence of the discrepant instability modes. Therefore, to quantitatively define the critical conditions of the involved instability modes in certain unstable non-parallel flows, the profile of the misaligned base flow velocity, usually in terms of cross/spanwise flow that is orthogonal to the designated streamwise flow, needs to be specified in the stability analysis. For a weak non-parallel flow, only the magnitudes of the base flow velocity are assumed to vary in both the transverse and vertical directions, *e.g.*, in a recent stability analysis²⁶. Nevertheless, for a strong non-parallel flow, *e.g.*, the JICF mentioned above, the profiles of the main stream flow (the boundary layer flow in the JICF) and transverse flow (the jet flow in the JICF) are usually needed to be specified in stability analysis²⁷⁻²⁹. Once the profiles are established, the quantitative influence of the cross shears is represented by the magnitude ratio between the jet and boundary layer flows. Such a velocity ratio is confirmed to be one of the governing parameters in the JICF²³. Similar to JICFs in engineering, our recent work³⁰ found that the cross shear in non-parallel free sheared flows, which usually occur in geophysical circumstances, also directly or indirectly leads to multiple instability modes, which are governed by the ratio between the base flow velocity and the perturbations in the spanwise direction.

However, in stabilization of a non-parallel flow, though the critical roles of the misaligned base flow and twisted shear are also confirmed, their modeling in hydrodynamics is rather implicit. To investigate the stabilization of the leading-edge vortex on a rotating flat plate, Wojcik & Buchholz³¹ indirectly included the stabilization from the spanwise velocity as a source term in the vorticity budget and named it as the ‘annihilation’ of vorticity. Though the ‘annihilation’ is solidified by the magnitude of the corresponding source term in the vorticity budget, how the spanwise velocity dynamically stabilizes the leading-edge vortex is still unclear. Similarly, the indirect influence of the spanwise velocity was confirmed by Jardin³², who studied the Coriolis effects on the stabilization of the leading-edge vortex. The author suggested that the Coriolis effects promote the spanwise flow in the core of and behind the leading-edge vortex, therefore stabilize the vortex structures atop the rotating boundary layer and prevent the detachment, yet how exactly the spanwise flow interacts and stabilizes the leading-edge vortex is still unknown. Some studies found that the stabilization associated with the misaligned base flow is relevant to the resultant twisted vortex structures. For example, the implication of the spanwise velocity on the stabilization of

This is the author's peer reviewed, accepted manuscript. However, the online version of record will be different from this version once it has been copyedited and typeset.

PLEASE CITE THIS ARTICLE AS DOI: 10.1063/1.50083687

bluff-body wakes was also elaborated by Hwang, Kim, & Choi¹⁹, who suggested that the overall vortex structures are significantly modified based on the vortex dynamics, in addition to the spanwise perturbations induced by surface waviness. Likewise, Guercvio, Cossu & Pujals³³ introduced the spanwise 'streaky wakes' as the spanwise modulations in the parallel base flow and found the amplitudes of such artificial wakes can completely suppress the absolute instability and convert it into a convective one. They attributed such effective stabilization mainly to the spanwise mean flow distortion.

Though some evidences noted above strongly indicate that the spanwise velocity directly or indirectly modifies the non-parallel base flow or the derived coherent structures, so that the overall non-parallelism appears more stable, yet, the shear of the spanwise velocity, named as the cross shear by Atsavapranee & Gharib²⁴, is insufficiently considered in hydrodynamic analysis, particularly compared to those studies on destabilization. Likewise, there should be a quantitative way to describe whether the stable cross shear is necessary in stabilization of the non-parallel flow and how it contributes to the overall stabilization. The answer to this primarily motivates the present study. In addition, with the consideration of the quantitative role of the cross shear, the potential interactions between the base flow distortions (misaligned base flow) and three-dimensional perturbations in the non-parallel flow can be investigated together, which also motivates the present study. After all, the majority of the non-parallel flows are more or less induced by both factors. Furthermore, as the previous studies^{19,33} on stabilization of different types of non-parallel flows confirm the involvement of the twisted vortex structures, the present study will further investigate how exactly the stable cross shear, together with the three-dimensional perturbations, contributes to the twisted vortex structures in the stabilization. At last, with the improved understanding of the role of the cross shear in stabilization, the present study may provide some preliminary implications to the applications of the stable cross shear in engineering scenarios that desire for stabilization, *e.g.*, by either actively or passively imposing the stable cross shear to locally stabilize the non-parallel flow.

Nevertheless, as reviewed above, the non-parallelism involving both the cross shear and the spanwise perturbations is inherently complicated, thus necessary simplifications are needed to focus on the role of the cross shear. To our best knowledge, so far there has been no hydrodynamic analysis on stabilization that considers the specific stable spanwise velocity and the cross shear. As a preliminary study, it is appropriate to focus on the linear

analysis, as the present study does. Specifically, the free sheared non-parallel flow (cross sheared flow, abbreviated as ‘CS flow’ hereafter) with the base flow represented by the following profiles is selected in the present study for the investigation of the stabilization effects via the cross shear,

$$U = \tanh(z), \quad V = \xi z^3, \quad (1)$$

in which U and V represent the streamwise and spanwise velocity, and z represents the vertical (height) coordinate in the Cartesian system. The velocity ratio $\xi = |V|/|U|$, where $|U|$ and $|V|$ represent the magnitudes of U and V , is a measure of the relative cross shear intensity, suitably named as the ‘cross shear ratio’, as V is orthogonal to U . Correspondingly, as V perfectly aligns with the spanwise direction, the spanwise wavenumber of the perturbations is named as the ‘orthogonal wavenumber’ in the subsequent context. For the unstable velocity U , the classic hyperbolic-tangent velocity profile $U = \tanh(z)$ is selected for two reasons; theoretically, because for the free sheared flow the linear temporal mode is sufficient to capture its essential instability features, and practically, the hyperbolic-tangent profile represents the prototype of the two sheared layer flows, which widely exist in the circumstances where the velocity shear experiences a significant change within a limited region, *e.g.*, the sheared stratified flow, the interface between the jet flow and the boundary flow, and other flows where the strong gradient of the velocity shear is involved. For the stable velocity V , the profile of $V = \xi z^3$ is setup as it satisfies the Rayleigh’s inflection point theorem but violates the Fjórtoft’s theorem³⁴ as $V''(V - V_{z=0}) = 6\xi z(\xi z^3 - 0) = 6\xi^2 z^4 \geq 0$ where $V_{z=0}$ is the value of V at $z = 0$, which is zero. The selection of $V = \xi z^3$ is mainly due to the limited choices available, because there is barely report on the linear analysis of the stable base flow alone, which inherently provides no solutions of the temporal growth rate. Perhaps this is also why the stabilization of a stable base flow velocity could only be measured in non-parallel flow, thus the previous studies on the stabilization, as reviewed above, are usually involved for the non-parallelism. Thus, we select $V = \xi z^3$ mainly based on whether a spanwise velocity violates the Rayleigh’s inflection point or the the Fjórtoft’s theorem. The simplicity of such an unstable spanwise velocity provides certain theoretical convenience. Overall, the selection of such a simply base flow aims to give a ‘minimum representation’ of non-parallel shear flow system, so that the influences of the cross shear and its interactions with the spanwise perturbations can be better clarified. The profiles and the first and second derivatives of the base flow (Eq. (1)) with several ξ values are shown in

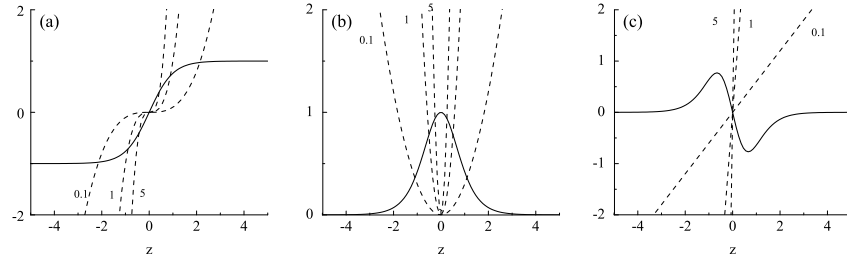


FIG. 1. (a) Schematic of the CS flow with $U = \tanh(z)$ (solid lines) and $V = \xi z^3$ (dash lines) with $\xi = 0.1, 1$ and 5 , and their first derivatives (b) and second derivatives (c).

Fig. 1.

To examine the role of the cross shear in the stabilization, in the present study, the overall stability of the CS flow (Eq. (1)) will be quantified first, by solving the eigenvalue problems described by the linearized perturbation equations. Accordingly, the solutions will provide the map of the unstable regions governed by a unique parameter that unifies the cross shear and the spanwise wavenumber. Subsequently, the dependence of stability on V will be studied. As will be described below, even for the linear stability model, the CS flow involves more complicated mechanisms, namely, the two distinctively different eigenfunction modes pertaining to the dominant roles of the orthogonal wavenumber and the cross shear, along with even more complicated transition in between the two eigenfunction modes. As the previous studies on stabilization^{19,31,33} suggested, the importance of vorticity distortion, the kinetic energy and enstrophy budgets in linearized forms will also be included in the examinations of eigenfunctions, in addition to the basic perturbations.

This paper is organized as follows. In Section II, the linearized perturbation equations and the procedures to solve the eigenvalue and the associated eigenfunctions, as well as the derived kinetic energy and vorticity perturbation budgets in the form of the normal modes are described in details. Section III presents the details of the eigenvalue/eigenfunction solver and the computational domain and the boundary conditions. Section IV presents the results of the eigenvalues/eigenfunctions of the CS flow, followed by the discussion and conclusions made in Section V.

II. LINEARIZED PERTURBATION EQUATIONS

It is assumed that the flow velocity vector $\vec{u}(\vec{x}, t)$ consist of the basic flow $\vec{U}(z)$ and the infinitesimal perturbation $\vec{u}'(\vec{x}, t)$, *i.e.*,

$$\vec{u}(\vec{x}, t) = \vec{U}(z) + \vec{u}'(\vec{x}, t), \quad (2)$$

where t is time, the components of \vec{x} are x , y and z , and the components of \vec{U} in the x , y and z directions are U , V and W and that of \vec{u}' are u' , v' and w' , respectively.

The dimensionless perturbation equations for an inviscid, incompressible and unstratified flow are as follows³⁵⁻³⁷,

$$\nabla \cdot \vec{u}' = 0, \quad (3)$$

$$\frac{\partial \vec{u}'}{\partial t} + (\vec{U} \cdot \nabla \vec{u}' + \vec{u}' \cdot \nabla \vec{U}) = -\frac{1}{\bar{\rho}} \nabla p', \quad (4)$$

where $\bar{\rho}$ is the reference density and p' is the perturbation part of the pressure away from the reference pressure corresponding to $\bar{\rho}$. All parameters are made dimensionless by their respective characteristic scales.

For the CS flow considered, both the primary and orthogonal base flow velocities are assumed to vary with the vertical coordinate z only, *i.e.*,

$$\vec{U}(z) = U(z)\vec{i} + V(z)\vec{j}. \quad (5)$$

Thus,

$$\begin{aligned} \vec{U} \cdot \nabla \vec{u}' &= \left(U \frac{\partial u'}{\partial x} + V \frac{\partial u'}{\partial y} \right) \vec{i} + \left(U \frac{\partial v'}{\partial x} + V \frac{\partial v'}{\partial y} \right) \vec{j} + \left(U \frac{\partial w'}{\partial x} + V \frac{\partial w'}{\partial y} \right) \vec{k}, \\ \vec{u}' \cdot \nabla \vec{U} &= w' \left(\frac{\partial U}{\partial z} \vec{i} + \frac{\partial V}{\partial z} \vec{j} \right). \end{aligned}$$

The following normal mode is used in the subsequent linear stability analysis,

$$\phi'(\vec{x}, t) = \hat{\phi}(z) e^{i(\alpha x + \beta y) - i\alpha c t} = \hat{\phi}(z) e^{i(\alpha x + \beta y) + \sigma t}, \quad (6)$$

where i is the imaginary unit of a complex number, α and β are the wavenumbers in the x and y directions, respectively, and the perturbation quantity ϕ' represents velocity, pressure or other physical quantities. The hat symbol $\hat{\phi}$ denotes the peak amplitude of the corresponding perturbation. c is the wave (phase) speed, which gives αc as the angular frequency for the perturbation, and $\sigma = -i\alpha c$ as the temporal growth rate of the perturbation.

Substituting the above normal modes into Eq. (3) and Eq. (4) leads to the following,

$$i\alpha\hat{u} + i\beta\hat{v} + D\hat{w} = 0, \quad (7)$$

$$(i\alpha U + i\beta V + \sigma)\hat{u} + U_z\hat{w} = -i\frac{1}{\rho}\alpha\hat{p}, \quad (8)$$

$$(i\alpha U + i\beta V + \sigma)\hat{v} + V_z\hat{w} = -i\frac{1}{\rho}\beta\hat{p}, \quad (9)$$

$$(i\alpha U + i\beta V + \sigma)\hat{w} = -\frac{1}{\rho}D\hat{p}, \quad (10)$$

where $D = \partial/\partial z$ is the differential operator for the perturbation properties, and the subscript 'z' denotes the first order differentiation with respect to z .

By applying the Squire transformations^{35,38}, the three-dimensional perturbation equations (7)-(10) can be reduced to (more details are presented in the Supplementary Materials),

$$\tilde{\sigma}\hat{w} = [-i\tilde{\alpha}(U\nabla_s^2 - U_{zz}) - i\frac{\tilde{\alpha}\beta}{\alpha}(V\nabla_s^2 - V_{zz})]\hat{w} \quad (11)$$

where

$$\tilde{\alpha} = (\alpha^2 + \beta^2)^{1/2}, \quad \tilde{\sigma} = \frac{\tilde{\alpha}}{\alpha}\sigma, \quad \nabla_s^2 = D^2 - \tilde{\alpha}^2,$$

in which the tilde symbol '~' denotes the Squire transformation properties, and the subscript 'zz' denotes the second order differentiation of the base flow velocity with respect to z . If $V = 0$ or $\beta = 0$, the perturbation equations for CS flows (Eq. (11)) will be reduced to the Rayleigh equation for the parallel sheared (PS) flow with $\alpha = \tilde{\alpha}$ inherently. On the other hand, if the composed velocity $\vec{U} = U\vec{i} + V\vec{j}$ aligns with the Squire wavenumber $\tilde{\alpha}$, so that the CS flow occurs in a single plane without any twists, Eq. (11) will also be reduced to the Rayleigh equation. However, if the profiles of U and V are different so that \vec{U} is twisted, \vec{U} will always misalign with the Squire wavenumber. The flow twists are represented by the term $(i\frac{\tilde{\alpha}\beta}{\alpha}V\nabla_s^2 - V_{zz})$ and therefore are determined by both the perturbation and the orthogonal velocity.

In Eq. (11), the terms $(\beta/\alpha)V$ and $(\beta/\alpha)V_{zz}$ unite the roles of ratio of the orthogonal wavenumber and the primary wavenumber β/α and the orthogonal velocity component V while solving the eigenvalue problems of $\tilde{\sigma}$, in spite of their distinctively physical differences. To distinguish the individual influences of β/α and ξ , the examination of the eigenfunctions is needed. As solving the eigenvalue problem of Eq. (11) also allows $\tilde{\sigma}$ and \hat{w} being solved,

the rest of the eigenfunctions \hat{u} , \hat{v} and \hat{p} can be established by substituting the obtained $\tilde{\sigma}$ and \hat{w} into Eqs. (7)-(9). For simplicity, $\bar{\rho} = 1$ is assumed in this study, so that $\hat{p}/\bar{\rho} = \hat{p}$.

After all basic eigenfunctions, *i.e.*, the perturbation fields are obtained, the kinetic energy ($e = \frac{1}{2}\overline{u_i'^2}$) budgets of the perturbation field for inviscid flow as shown below³⁶, can be obtained,

$$\frac{\partial e}{\partial t} + \bar{u}_j \frac{\partial e}{\partial x_j} = P_k + T_k + \Pi_k, \quad (12)$$

where

$$P_k = -\overline{u_i' u_j' \frac{\partial \bar{u}_i}{\partial x_j}}, \quad T_k = -\frac{\partial \overline{u_j' e'}}{\partial x_j}, \quad \Pi_k = -\frac{1}{\bar{\rho}} \frac{\partial \overline{p' u_j'}}{\partial x_j},$$

in which $e' = \frac{1}{2}u_i'^2$, P_k is the shear production of e via deformation work, T_k and Π_k describe the transports of e by the velocity and pressure perturbations, respectively.

As all the perturbations are assumed in the normal mode with the form of Eq. (6), for the homogeneous free-sheared flow studied in this paper, the product of two random perturbations yields,

$$\phi'(\vec{x}, t) \overline{\phi'(\vec{x}, t)} = \hat{\phi}(z) \hat{\phi}(z) e^{2i(\alpha x + \beta y) + 2\sigma t}, \quad (13)$$

as all perturbations share the same wavenumbers $\tilde{\alpha}$ and $\tilde{\beta}$ as well as the same grow rate $\tilde{\sigma}$. The average operation of the product $\overline{\phi'(\vec{x}, t) \phi'(\vec{x}, t)}$ is defined at one wavelength of $2\pi/\alpha$ and $2\pi/\beta$ in the primary and orthogonal directions, respectively, as follows,

$$\begin{aligned} \overline{\phi'(\vec{x}, t) \phi'(\vec{x}, t)} &= \int_0^{\frac{2\pi}{\alpha}} \frac{\alpha}{2\pi} \int_0^{\frac{2\pi}{\beta}} \frac{\beta}{2\pi} \hat{\phi}(z) \hat{\phi}(z) e^{2[i(\alpha x + \beta y) + \sigma t]} dx dy \\ &= \frac{\alpha\beta}{4\pi^2} \hat{\phi}(z) \hat{\phi}(z) e^{2\sigma t} \int_0^{\frac{2\pi}{\alpha}} \int_0^{\frac{2\pi}{\beta}} e^{2i(\alpha x + \beta y)} dx dy \\ &= \epsilon(x, y, t) \hat{\phi}(z) \hat{\phi}(z), \end{aligned} \quad (14)$$

in which

$$\epsilon(x, y, t) = \frac{\alpha\beta}{4\pi^2} e^{2\sigma t} \int_0^{\frac{2\pi}{\alpha}} \int_0^{\frac{2\pi}{\beta}} e^{2i(\alpha x + \beta y)} dx dy.$$

Every term in Eq. (12) includes the same integration term $\int_0^{\frac{2\pi}{\alpha}} \int_0^{\frac{2\pi}{\beta}} e^{2i(\alpha x + \beta y)} dx dy$ which can be canceled with each other.

By applying Eq. (14) to Eq. (12) yields the following kinetic energy budget of the perturbations in the normal mode form (more details are presented in the Supplementary Materials),

$$\sigma(\hat{u}^2 + \hat{v}^2 + \hat{w}^2) + (i\alpha U + i\beta V)(\hat{u}^2 + \hat{v}^2 + \hat{w}^2) = \hat{P}_{k,u} + \hat{P}_{k,v} + \hat{\Pi}_k, \quad (15)$$

in which

$$\hat{P}_{k,u} = -\hat{u}\hat{w}U_z, \quad \hat{P}_{k,v} = -\hat{v}\hat{w}V_z, \quad \hat{\Pi}_k = -i2(\alpha\hat{p}\hat{u} + \beta\hat{p}\hat{v}) - D(\hat{p}\hat{w}),$$

where \hat{T}_k is eliminated due to the term $\hat{u}_j\hat{e} = \hat{u}_j\hat{u}_i\hat{u}_i$, in which one integration $\int_0^{\frac{2\pi}{\alpha}} \int_0^{\frac{2\pi}{\beta}} e^{i(\alpha x + \beta y)} dx dy$ is unable to be canceled, but it is zero. The physical meanings of \hat{P}_k and $\hat{\Pi}_k$ are the same as P_k and Π_k , as they are just in the normal mode form. The influences of U and V on \hat{P}_k are separated into the U -oriented term $\hat{P}_{k,u}$ and the V -oriented term $\hat{P}_{k,v}$ for analytical conventions. As all eigenfunctions are complex numbers, the conservation of Eq. (15) is satisfied only for the real/imaginary part but not for the magnitudes of the complex properties.

Another parameter, called *enstrophy* and defined as $\frac{1}{2}\overline{\omega_i^2}$, can be introduced through vorticity perturbations to represent the twisted features of the CS flow³⁶. The vorticity perturbations are as follows,

$$\omega'_x = \frac{\partial w'}{\partial y} - \frac{\partial v'}{\partial z}, \quad \omega'_y = \frac{\partial u'}{\partial z} - \frac{\partial w'}{\partial x}, \quad \omega'_z = \frac{\partial v'}{\partial x} - \frac{\partial u'}{\partial y}. \quad (16)$$

By applying the normal modes yields the following,

$$\hat{\omega}_x = i\beta\hat{w} - D\hat{v}, \quad \hat{\omega}_y = D\hat{u} - i\alpha\hat{w}, \quad \hat{\omega}_z = i\alpha\hat{v} - i\beta\hat{u}. \quad (17)$$

The enstrophy budget of the perturbation field for the invicid sheared flow considered in this paper is as follows³⁶,

$$\frac{\partial}{\partial t} \left(\frac{1}{2}\overline{\omega^2} \right) + \overline{u_j} \frac{\partial}{\partial x_j} \left(\frac{1}{2}\overline{\omega^2} \right) = P_\omega + T_\omega + S_\omega, \quad (18)$$

where

$$P_\omega = -\overline{u'_j \omega'_i} \frac{\partial \overline{\omega_i}}{\partial x_j}, \quad T_\omega = -\frac{\partial}{\partial x_j} \overline{u'_j} \left(\frac{1}{2}\overline{\omega_i^2} \right), \quad S_\omega = \overline{\omega'_i \omega'_j s'_{ij}} + \overline{\omega'_i \omega'_j \overline{s}_{ij}} + \overline{\overline{\omega}_i \omega'_j s'_{ij}}.$$

P_ω is the gradient production of enstrophy via the exchange between the basic flow and the perturbed vorticity field, T_ω is the transport of enstrophy by the velocity perturbation, S_ω is the stretching of the vortex by the perturbation deformation field $\overline{s'_{ij}}$, the average deformation field \overline{s}_{ij} and the average vorticity field $\overline{\omega}_i$. The rate of strain tensor is defined as follows,

$$s'_{ij} = \frac{1}{2} \left(\frac{\partial u'_i}{\partial x_j} + \frac{\partial u'_j}{\partial x_i} \right). \quad (19)$$

By applying Eq. (14) to Eq. (18), the enstrophy budget of the perturbations in the normal mode form, after both sides are divided by $2\epsilon(x, y, t)$, becomes,

$$(\sigma + i\alpha U + i\beta V)(\hat{\omega}_x^2 + \hat{\omega}_y^2 + \hat{\omega}_z^2) = \hat{P}_{\omega,u} + \hat{P}_{\omega,v} + \hat{S}_{\omega,1,u} + \hat{S}_{\omega,1,v} + \hat{S}_{\omega,2,u} + \hat{S}_{\omega,2,v}, \quad (20)$$

in which

$$\begin{aligned}
\hat{P}_{\omega,u} &= -U_{zz}(\hat{w}D\hat{u} - i\alpha\hat{w}^2), & \hat{P}_{\omega,v} &= -V_{zz}(\hat{w}D\hat{v} - i\beta\hat{w}^2), \\
\hat{S}_{\omega,1,u} &= \hat{\omega}_x\hat{\omega}_zU_z, & \hat{S}_{\omega,1,v} &= \hat{\omega}_y\hat{\omega}_zV_z, \\
\hat{S}_{\omega,2,u} &= U_z(\hat{\omega}_x\hat{s}_{yx} + \hat{\omega}_y\hat{s}_{yy} + \hat{\omega}_z\hat{s}_{yz}) \\
&= \frac{1}{2}U_z(i\beta\hat{\omega}_x\hat{u} + i\alpha\hat{\omega}_x\hat{v} + 2i\beta\hat{\omega}_y\hat{v} + \hat{\omega}_zD\hat{v} + i\beta\hat{\omega}_z\hat{w}), \\
\hat{S}_{\omega,2,v} &= -V_z(\hat{\omega}_x\hat{s}_{xx} + \hat{\omega}_y\hat{s}_{xy} + \hat{\omega}_z\hat{s}_{xz}) \\
&= -\frac{1}{2}V_z(2i\alpha\hat{\omega}_x\hat{u} + i\beta\hat{\omega}_y\hat{u} + i\alpha\hat{\omega}_y\hat{v} + \hat{\omega}_zD\hat{u} + i\alpha\hat{\omega}_z\hat{w}),
\end{aligned}$$

where \hat{T}_ω is eliminated as the same as \hat{T}_k because of the term $\hat{u}\hat{\omega}_i\hat{\omega}_i$. \hat{P}_ω and \hat{S}_ω inherit the physical meanings of P_ω and S_ω as they are just in the normal mode form. To facilitate the analysis in the following sections, both \hat{P}_ω and \hat{S}_ω are subdivided into the U and V related sub-terms as indicated by the third subscripts 'u' and 'v'. For \hat{S}_ω , the term $\hat{\omega}_i\hat{\omega}_j\hat{s}_{ij}$ is also eliminated, and the rest terms involving \bar{s}_{ij} and \hat{s}_{ij} are also separated and indicated by the second subscripts '1' and '2'. As all eigenfunctions in Eq. (20) are complex numbers, the conservation of Eq. (20) is also satisfied only for the real/imaginary part, not for the magnitudes of the complex properties.

III. METHODOLOGY

The temporal mode of the eigenvalue problems (11) is solved with the matrix methods. The linearized perturbation equation (11) is uniformly discretized by using the second-order central difference scheme. The QZ algorithm developed by Moler & Stewart³⁹, which is integrated in the Linear Algebra package (LAPACK) routine CGGEV, is used as the complex eigenvalue solver. The robustness of the QZ algorithm in the hydrodynamic stability analysis has been demonstrated in some studies (*e.g.*, Liu, Thorpe & Smyth⁴⁰, Smyth, Moum & Nash⁴¹, Thorpe, Smyth & Li⁴²). With the QZ algorithm, solving the eigenvalue problem (11) also obtains \hat{w} . As both σ and \hat{w} are solved, Eqs. (7)-(9) are used to solve the rest unknown eigenfunctions \hat{u} , \hat{v} and \hat{p} with the solver ZSYSV integrated in the LAPACK. After all basic eigenfunctions associated to the eigenvalue σ are obtained, the related terms to the kinetic energy and enstrophy budgets Eq. (15) and Eq. (20) are computed.

The boundary conditions $u = w = v = 0$ are applied at both the top and the bottom boundaries. The dimensionless vertical coordinate z varies between -5 and 5 , giving the cor-

responding dimensional computational domain a size ten times of the characteristic length. The resolution with node numbers of 600 \sim 2000 as well as the dimensionless computational domain sizes between 10 and 50 are tested, with less than 1% variations observed. Thus 10 is selected as the dimensionless computational size along with the node number of 600, which is sufficiently large to capture the asymptotic hydrodynamic behaviors obtained in other settings with the much larger domain sizes and many more node numbers.

IV. RESULTS

A. Unstable region - its boundary and the path of the maximum growth rate

With the above base flow, $(\beta/\alpha)V$ and $(\beta/\alpha)V_{zz}$ in Eq. (11) become $(\beta/\alpha)\xi z^3$ and $6(\beta/\alpha)\xi z$, respectively, so that the velocity (cross shear) ratio ξ and the orthogonal wavenumber ratio β/α are combined into a single factor $\chi = (\beta/\alpha)\xi$, which determines the eigenvalue $\tilde{\sigma}$ regardless of the relative ratio between β/α and ξ . Figure 2 plots the temporal growth rate $\tilde{\sigma}$ against the Squire wavenumber $\tilde{\alpha}$ for different χ values. For $\chi = 0$, the CS flow of Eq. (1) reduces to the PS flow of $U = \tanh(z)$ and the values of the wavenumber $\tilde{\alpha}_{max}$ where the maximum $\tilde{\sigma}$ occurs on the dispersion relation is around 0.45 \sim 0.46, which agrees with the results obtained by the shooting methods and other spectrum methods^{37,43-45}. After non-zero χ is introduced and increased, the curve signifying the dispersion relation begins to shrink significantly and $\tilde{\alpha}_{max}$ reduces. Further increase of χ leads to $\tilde{\alpha}_{max}$ approaching 0.1. As χ increases to more than 0.14, none of the $\tilde{\sigma} \neq 0$ solution is obtained, indicating that the stability boundary is reached. The drastic falling of the dispersion curves by increasing χ exhibits obviously the stabilized effect of the orthogonal velocity component V , which proves that introducing a stable V profile can indeed stabilize the whole CS flow.

To gain a comprehensive perspective of how V stabilizes the CS flow (Eq. (1)), the stability boundary, *i.e.*, the contour of $\tilde{\sigma} = 0$, is plotted in Fig. 2(b), along with the path of the maximum growth rate $\tilde{\sigma}_{max}$ inside the unstable regions. Every $\tilde{\sigma}_{max}$ for a given χ is searched from the corresponding curve of dispersion relation, and accordingly the corresponding wavenumber $\tilde{\alpha}_{max}$ where $\tilde{\sigma}_{max}$ occurs is recorded as well. Consequently, a series of $(\tilde{\alpha}_{max}, \chi)$ pairs are plotted in Fig. 2(b) and form the path of $\tilde{\sigma}_{max}$, where $\tilde{\sigma}_{max}$ decreases as χ increases as indicated by the arrow. It should be noted that the stability boundary in

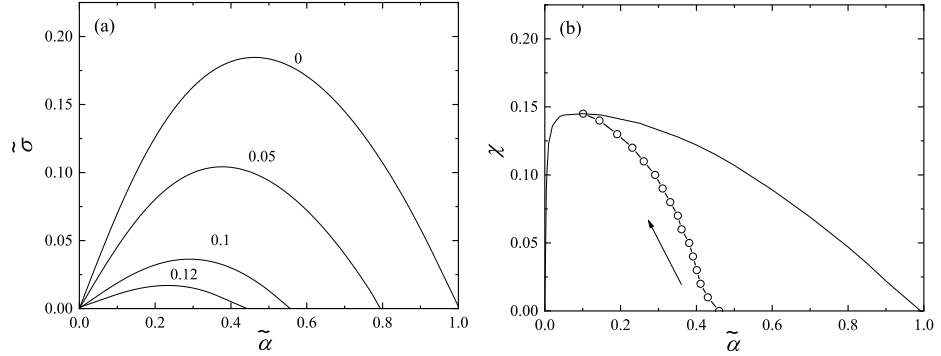


FIG. 2. (a) The growth rate $\tilde{\sigma}$ plotted against the Squire wavenumber $\tilde{\alpha}$ with different χ values and (b) the contour of $\tilde{\sigma} = 0$ (solid line) as well as the path of the maximum growth rate $\tilde{\alpha}_{max}$ (void circles) of different dispersion curves in terms of χ versus $\tilde{\alpha}$ for the CS flow (Eq. (1)). The arrow in (b) denotes the decrease of $\tilde{\alpha}_{max}$ with increasing χ .

Fig. 2(b) is unique in that it only exists when the V profile is stable and $\chi \neq 0$. That is to say, as $\chi = (\beta/\alpha)\xi$, non-zero ξ , even with a negligible magnitude, is a necessary condition for the stabilization of the CS flow, regardless how large β/α is. The necessity of stable V agrees with the indirect but necessary role of spanwise velocity with significant spanwise perturbations found in previous studies^{19,33}. The maximum χ on the stability boundary is $\chi_{cr} \approx 0.145$, whose role is similar to the critical Richardson number $Ri_{cr} = 0.25$ for the stratified PS flow. Unlike the stability boundary created by the stratification, *e.g.*, as computed by Hazel⁴⁴ and Smyth & Peltier⁴⁵, the wavenumber at which $\tilde{\sigma}_{max}$ occurs also significantly shifts along the $\tilde{\sigma}_{max}$ path, *e.g.*, from $\tilde{\alpha} \approx 0.46$ at $\chi = 0$ to $\tilde{\alpha} \approx 0.1$ at $\chi = 0.14$, which indicates that the overall length scale of the instability on the path of $\tilde{\sigma}_{max}$ will increase with increased χ during the decay stage. This is supported by the subsequent eigenfunction results.

B. Eigenfunctions

As a perturbation property and a measure of the background shear, β/α and ξ inherently indicate distinctively different physical situations. If $\beta/\alpha \gg \xi$, the perturbation structures,

namely, the eigenfunction structures, might be close to the ones where $U \gg V$ with $\beta \gg \alpha$, leading to the ‘orthogonal wavenumber’ (OW) eigenfunction mode. On the other hand, if $\xi \gg \beta/\alpha$, the perturbation structures may be determined by the cross shear from the V profile, resulting in the ‘cross shear’ (CS) eigenfunction mode. The two extreme cases correspond to two fundamental eigenfunction modes in the CS flow for each fixed χ . As β/α and ξ are mostly in finite magnitudes, the eigenfunctions are a mixture of the two extreme modes, which corresponds to a ‘hybrid’ eigenfunction mode.

As unified by χ , the influences of β/α and ξ are concealed by the eigenvalue problems. To further examine the individual influences of β/α and ξ and their associated OW and CS modes, the basic eigenfunctions and their derived budgets of Eq. (15) and Eq. (20) are needed. In addition, to quantify the relative role of β/α and ξ , a ratio $\psi = (\beta/\alpha)/\xi$ is defined to indicate the critical conditions of the OW, CS and hybrid modes. Moreover, as the path of $\tilde{\sigma}_{max}$ indicates the gradient of $\tilde{\sigma}$ within the whole unstable regions as shown in Fig. 2(b), it is both mathematically and physically reasonable to select the eigenfunctions on the path of $\tilde{\sigma}_{max}$ as the representatives of the entire unstable region. For convenience, the path of $\tilde{\sigma}_{max}$ will be called ‘the path’ in the rest of the paper.

1. The OW mode

Figure 3 presents the profiles of the basic eigenfunctions in the z direction with $\chi = 0.06$ at $\psi = 600$, *i.e.*, \hat{u} , \hat{w} , \hat{p} , $\hat{\omega}_x$, \hat{v} and $\hat{\omega}_y$ as well as the products $\hat{u}\hat{w}$, $\hat{p}\hat{w}$, $D(\hat{p}\hat{w})$, $\hat{\omega}_x\hat{\omega}_z$ and $\hat{\omega}_y\hat{\omega}_z$ that have significant influences on the kinetic energy/enstrophy budget. For comparison, the results for the eigenfunctions associated with the PS flow of $U = \tanh(z)$ with $\chi = 0$ are also plotted.

From this figure, it is seen that overall, for the OW mode, the majority of the profiles of the basic eigenfunctions in the z direction vary within $z \in [-2, 2]$ where the major variations of the primary shear $U_z = \text{sech}^2(z)$ and $U_{zz} = -2\tanh(z)\text{sech}^2(z)$ occur, rather than the entire domain of $z \in [-5, 5]$ on which the orthogonal shear $V_z = 3z^2$ and $V_{zz} = 6z$ have influences. Such confined regions of $z \in [-2, 2]$ indicate that the primary shear remains critical in the OW mode. Under such critical influence of the primary shear, some basic eigenfunctions, *e.g.*, \hat{u} , \hat{w} as well as their product term $\hat{u}\hat{w}$ shown in the first row of Fig. 3, develop similar symmetrical features and magnitudes to those associated with $U = \tanh(z)$.

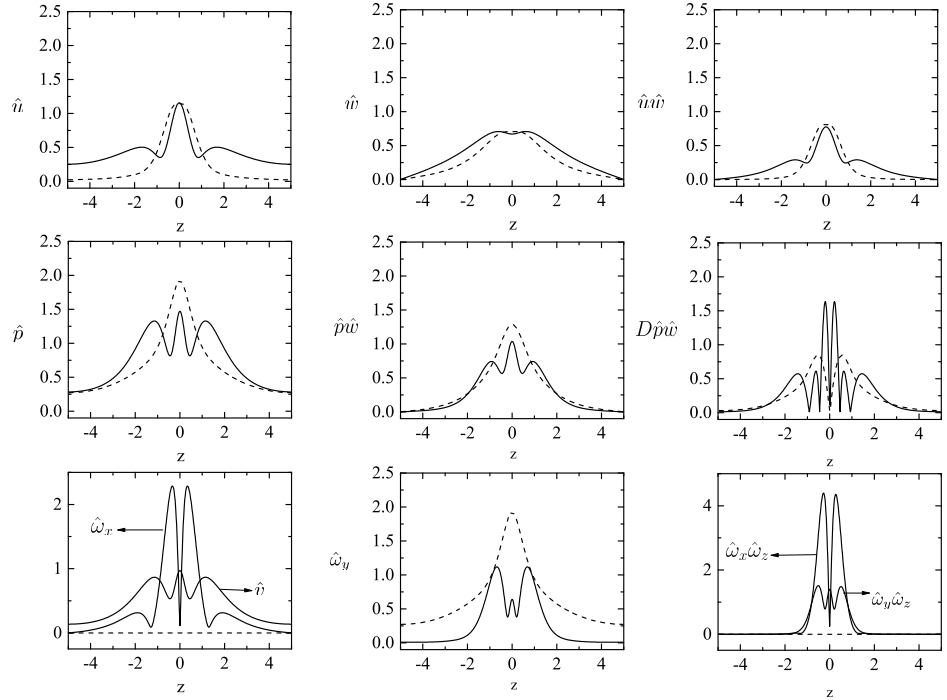


FIG. 3. The profiles of the absolute values of \hat{u} , \hat{w} , $\hat{u}\hat{w}$, \hat{p} , $\hat{p}\hat{w}$, $D(\hat{p}\hat{w})$, $\hat{\omega}_x$ and \hat{v} , $\hat{\omega}_y$, and $\hat{\omega}_x\hat{\omega}_z$ and $\hat{\omega}_y\hat{\omega}_z$ in the z direction, with $\psi = 600$ at $\chi = 0.06$ (solid lines) and $\chi = 0$ (dashed lines), respectively.

Yet, due to the flow twist in terms of $\beta/\alpha \gg \xi$ in the OW mode, some deformations compared to the PS flow of $U = \tanh(z)$ are found, *e.g.*, \hat{p} of the OW mode involves a triple-peak profile so that the related product $\hat{p}\hat{w}$ and $D(\hat{p}\hat{w})$ appear to be quite different from those associated with the PS flow. These scattered eigenfunction structures in terms of multiple peaks are apparently attributed to the reduced wavelength of perturbations due to the dominant role of β/α in the OW mode. The features of multiple peaks in the OW mode further complicate the transportation and productions of the kinetic energy/enstrophy as will be shown later. The most deviated feature of the OW mode is the significant non-zero values of $\hat{\omega}_x$ and \hat{v} . In the PS flow, the perfect alignment between the perturbations and the base flow gives rise to little perturbations in the orthogonal direction and therefore

result in zero \hat{v} and $\hat{\omega}_x$. On the contrary, the misalignment between the Squire wavenumber and the base flow forces the perturbations to develop in both the primary and orthogonal directions, leading to significant non-zero values of $\hat{\omega}_x$ and \hat{v} in the orthogonal direction. Nevertheless, for the OW mode, the misalignment is mainly caused by β/α as $\beta/\alpha \gg \xi$, as a result the magnitudes of \hat{v} are less than those of $\hat{\omega}_x$ as $\hat{\omega}_x = i\beta\hat{w} - D\hat{v}$ is augmented by β . The contributions of \hat{v} to the kinetic energy/enstrophy budget are further substantially compromised by the suppressed cross shear V_z owing to $(\beta/\alpha) \gg \xi$ in the OW mode. The suppressed cross shear also enlarges the gap between $\hat{\omega}_x\hat{\omega}_z$ and $\hat{\omega}_y\hat{\omega}_z$ in the enstrophy budget, thereby introducing new structures that never exist in the PS flow as will be shown later.

Figure 4 shows the eigenfunctions of the kinetic energy and enstrophy budgets at $\chi = 0$ and $\chi = 0.06$, both with fixed $\psi = 600$. Compared to the PS flow ($\chi = 0$), for the CS flow ($\chi = 0.06$), due to the deformations of \hat{p} and its associated product, *e.g.*, $\hat{p}\hat{w}$, the eigenfunctions of $\hat{\Pi}_k$, namely, the transportation of the kinetic energy via the pressure gradient, display the dominant quadruple-peak profiles as shown in Fig. 4(c), indicating that the flow structures are twisted at several scattered regions. At the approximately same positions where the quadruple peaks of $\hat{\Pi}_k$ occur, in Fig. 4(d) the twin-peak structures of $\hat{S}_{\omega,u,1}$, $\hat{S}_{\omega,u,2}$ and $\hat{P}_{k,u}$ occur and represent the twisted effects in the enstrophy budget. The existences of $\hat{S}_{\omega,u,1}$ and $\hat{S}_{\omega,u,2}$ are unique for the CS flow, because for the PS flow, the alignment between the base flow and perturbations inherently eliminates vortex stretching via the rate of the strain in the linear instability.

The diminished length scales due to β/α with $\beta/\alpha \gg \xi$ in the OW mode are demonstrated by the profiles of $\hat{\Pi}_k$, $\hat{S}_{\omega,u,1}$, $\hat{S}_{\omega,u,2}$ shown in Fig. 4. Nonetheless, they do not necessarily lead to stabilization, as the reduced/scattered length scales are also observed in destabilization of the non-parallel flows. For instance, with spanwise perturbations, a similar streamwise velocity U applied in this study can also create a series of unstable spanwise vortex structures with reduced length scales, as what Atsavapranee & Gharib²⁴ and Lin *et al.*²⁵ experimentally and numerically investigated. The similar destabilization via the spanwise wavenumber can also be found in numerous studies on the JICF²³. Then why can some studies, *e.g.*,^{9,19,26}, still achieve stabilization by introducing spanwise perturbations? We still suggest that the stable V and the associated cross shear is the key mechanism behind the stabilization of the OW mode. The evidence is the weak but not negligible presence of the twin-peak structures of $\hat{P}_{k,v}$ confined in $z \in [-1, 1]$ shown in Fig. 4(d). Thus, the stabilization from cross shear

This is the author's peer reviewed, accepted manuscript. However, the online version of record will be different from this version once it has been copyedited and typeset.

PLEASE CITE THIS ARTICLE AS DOI: 10.1063/1.50083687

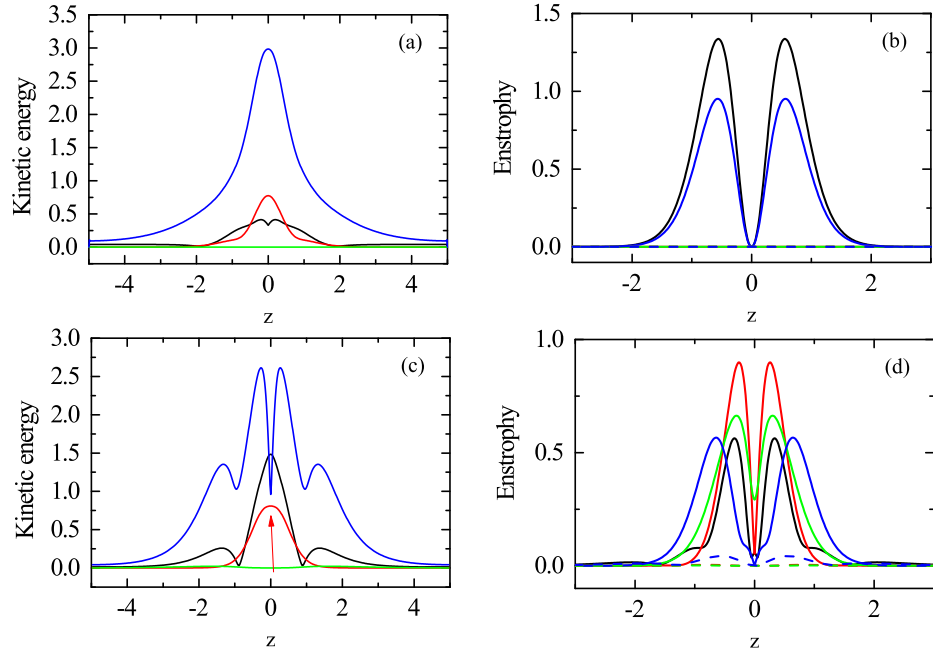


FIG. 4. The profiles of the absolute values of the kinetic energy budget (left column) and the enstrophy budget (right column) of the perturbations for the CS flow (1) at $\chi = 0$ (a)–(b) and $\chi = 0.06$ (c)–(d), both with $\psi = 600$, in the z direction. For the kinetic energy budget, (—), (—), (—) and (—) denote $D\hat{e}/Dt$, $\hat{P}_{k,u}$, $\hat{P}_{k,v}$ and $\hat{\Pi}_k$; for the enstrophy budget, (—), (—), (—), (—), (---), (---), and (---) denote $D\hat{\omega}^2/Dt$, $\hat{S}_{\omega,u,1}$, $\hat{S}_{\omega,u,2}$, $\hat{P}_{\omega,u}$, $\hat{S}_{\omega,v,1}$, $\hat{S}_{\omega,v,2}$ and $\hat{P}_{\omega,v}$, respectively.

on vortex deformation is not negligible, even V is negligible in the OW mode.

The limited regions of the twin-peak structures of $\hat{P}_{k,v}$ also determine how the stabilization is achieved in the OW mode. Figure 5 shows the profiles of the eigenfunction \hat{p} at $\chi = 0.06$, 0.09 and 0.14 along the path at $\psi = 1000$ for the OW mode. A clear decay of the triple-peak structures of \hat{p} can be observed as ψ increases along the path. Particularly, as indicated by the arrows, the overall structures of \hat{p} shrink towards the central region at $z \in [-1, 1]$, the same position where the twin-peak structures of $\hat{P}_{k,v}$ occur shown in Fig. 4(d). Meanwhile,

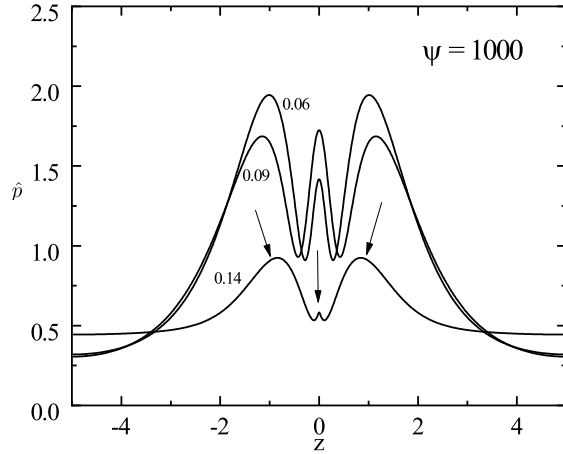


FIG. 5. The profiles of the absolute value of \hat{p} at $\psi = 1000$ with $\chi = 0.06$, 0.09 and 0.14 , respectively. The arrows indicate the decay of \hat{p} .

the central peak of \hat{p} ostensibly decays with increased χ and is almost annihilated at $\chi = 0.14$ very near the stability boundary. Thus, such a decay fashion of \hat{p} suggests that it is the cross shear which stabilizes the pressure perturbations. As the sheared CS flow is pressure-driven, \hat{p} provides momentum for the perturbed velocity as well as vorticity, therefore the stabilization of \hat{p} at last leads to the overall stabilization of the CS flow as χ increases along the path.

2. The CS mode

Figure 6 shows the eigenfunctions of \hat{v} and \hat{u} , $\hat{v}\hat{w}$ and $\hat{u}\hat{w}$, $\hat{\omega}_x$ and $\hat{\omega}_y$, $\hat{\omega}_z$ and $\hat{\omega}_y\hat{\omega}_x$, $\hat{\omega}_x\hat{\omega}_y$, and $\hat{\omega}_y\hat{\omega}_z$ with $\psi = 1/600$ at $\chi = 0.06$. Similar to the OW mode, the misalignment between the base flow and the perturbations leads to the twisted features of the eigenfunctions, *e.g.*, the non-zero \hat{v} , $\hat{\omega}_x$ and $\hat{\omega}_z$. Nevertheless, as a result of $\xi \gg (\beta/\alpha)$, the twisted features of the CS mode are extremely inclined to the orthogonal direction. For instance, the cross shear directly produces absolutely dominant \hat{v} in the orthogonal directions over \hat{u} in the primary direction. Accordingly, the dominant \hat{v} significantly increases the magnitudes of $\hat{\omega}_x$ and $\hat{\omega}_z$, so that $\hat{\omega}_y$ exerts very little influences. In addition, the profiles of \hat{v} and $\hat{\omega}_x$ extend across

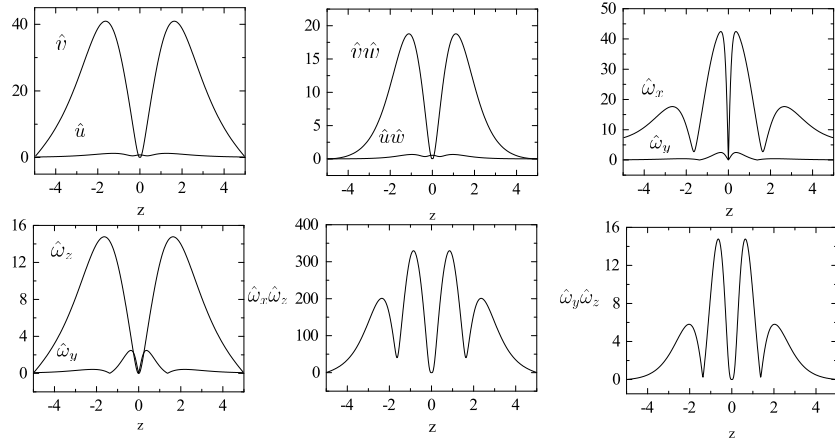


FIG. 6. The profiles of the absolute values of \hat{v} and \hat{u} , $\hat{v}\hat{w}$ and $\hat{u}\hat{w}$, $\hat{\omega}_x$ and $\hat{\omega}_y$, $\hat{\omega}_z$ and $\hat{\omega}_y\hat{\omega}_z$, and $\hat{\omega}_x\hat{\omega}_z$ in the z direction, with $\psi = 1/600$ at $\chi = 0.06$.

the entire domain, which agrees with the extensions of the cross shear $U_z = \text{sech}^2(z)$ and $U_{zz} = -2\tanh(z)\text{sech}^2(z)$ in the z direction as shown in Fig. 1. Hence, the stabilization also extends across the entire domain, unlike those associated with the OW mode and the PS flow that are limited within the region $z \in [-2, 2]$ where the primary shear mostly varies.

The extended eigenfunctions developed in favor of the orthogonal direction, *i.e.*, \hat{v} as well as the associated $\hat{\omega}_x$ and $\hat{\omega}_z$, also introduce similar features of the related product terms, *e.g.*, $\hat{v}\hat{w}$, $\hat{\omega}_x\hat{\omega}_z$, and $\hat{\omega}_y\hat{\omega}_z$. These product terms with significant magnitudes directly contribute to the cross shear-determined eigenfunctions of the kinetic energy and enstrophy budgets in the CS mode as shown in Fig. 7. Specially, the kinetic energy is basically all produced by the twin-peak structure of $\hat{P}_{k,v}$, which spans over the entire domain as shown in the figure. For the enstrophy budget, in addition to their extended span in the z direction compared to the OW mode, the multiple-peak structures, *e.g.*, of $\hat{S}_{\omega,v,1}$, $\hat{S}_{\omega,v,2}$, and $\hat{P}_{\omega,v}$, are observed, which distinguish the features of the CS mode with that of the OW mode.

To demonstrate the stabilization in the CS mode, Fig. 8 shows the profile \hat{p} as a function of ψ along the path at $\psi = 0.1$. It should be emphasized that there are little changes for the \hat{p} profile as ψ further increases beyond 0.1. As the cross shear in terms of $\hat{S}_{\omega,v,1}$, $\hat{S}_{\omega,v,2}$, and

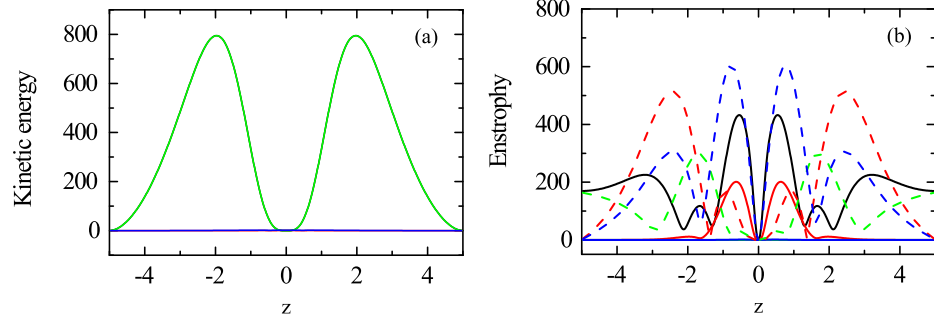


FIG. 7. The profiles of the absolute values of (a) the kinetic energy budget and (b) the enstrophy budget of the perturbations in the z direction for the CS flow with $\psi = 1/600$ and $\chi = 0.06$. For the kinetic energy budget (left column), (—), (—), (—), and (—) denote $D\hat{e}/Dt$, $\hat{P}_{k,u}$, $\hat{P}_{k,v}$, and $\hat{\Pi}_k$; for the enstrophy budget, (—), (—), (—), (—), (---), (---), and (---) denote $D\hat{\omega}^2/Dt$, $\hat{S}_{\omega,u,1}$, $\hat{S}_{\omega,u,2}$, $\hat{P}_{\omega,u}$, $\hat{S}_{\omega,v,1}$, $\hat{S}_{\omega,v,2}$, and $\hat{P}_{\omega,v}$, respectively.

$\hat{P}_{\omega,v}$ almost occurs across the entire vertical domain as shown in Fig. 7(b), the profile of \hat{p} is also stabilized everywhere, as the gradient $\partial\hat{p}/\partial z$ is significantly decreased when χ increases from 0.06 to 0.14. Meanwhile, because the destabilizing influence of the primary shear is weak but still exists in terms of the central twin-peak structures of $\hat{S}_{\omega,u,1}$ shown in Fig. 7(b), the central peak of \hat{p} is kept. Yet, as χ increases along the path, the gradient $\partial\hat{p}/\partial z$ near the central peak is still significantly compromised. In general, unlike the OW mode, the stabilization in the CS mode via the cross shear is achieved by deteriorating the gradient $\partial\hat{p}/\partial z$ across the entire vertical domain. The primary shear remains but in a very limited central region to sustain the destabilization of the CS flow. Once χ reaches the stability boundary, the gradient $\partial\hat{p}/\partial z$ sustained by the primary shear is destroyed at last.

3. The transition

The OW mode and the CS mode are in fact two extreme cases where $(\beta/\alpha) \gg \xi$ and $(\beta/\alpha) \ll \xi$, respectively. When β/α and ξ are comparable, the features of both the OW mode and the CS mode described above may coexist, leading to a ‘hybrid’ mode. In this section, the transition among the OW, the CS and the hybrid modes is examined with the

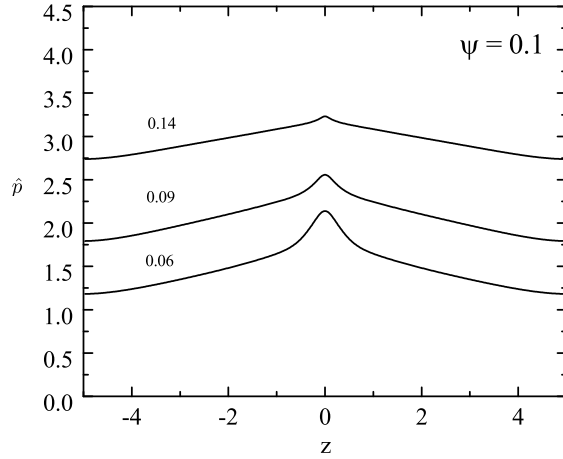


FIG. 8. The profiles of the absolute value of \hat{p} at $\psi = 0.1$ with $\chi = 0.06, 0.09$ and 0.14 , respectively.

varying relative ratio $\psi = (\beta/\alpha)/\xi$, which also quantifies the effective regions where the OW mode, the CS mode and the hybrid mode exist.

Figure 9 shows the eigenfunctions of the enstrophy budget at fixed $\chi = 0.06$ and several ψ values, while Fig. 10 (Multimedia view) presents the results for more ψ values over $\psi = 0.001 \sim 10000$ at fixed $\chi = 0.06$, which demonstrates the entire transitions. It is observed that in general the transitions involve three stages. In the first stage, from $\psi = 10000$ to 10 , the initial eigenfunctions of the OW mode increase their magnitudes as ψ decreases, with, noticeably, the merger of the twin-peaks of $\hat{S}_{\omega,u,1}$ into a single-peak structures as shown in Fig. 9(a)-(c). After the merger, the new central peak structure of $\hat{S}_{\omega,v,1}$ begins to decay further when ψ decreases to below 10 as shown in Fig. 9(d), as both its magnitude and the span in the z direction decrease with decreased ψ . The deformations of other eigenfunctions associated with the OW mode are also observed when ψ decreases from 10000 to 10 , indicating that it is not only the enstrophy budget but the whole OW mode are modified during the first transitional stage as ψ decreases. The mechanisms behind this first transitional stage will be discussed later with the variation of \hat{p} . The second stage begins from $\psi = 2$, in which the eigenfunctions signifying the CS mode, *i.e.*, $\hat{S}_{\omega,v,1}$, $\hat{S}_{\omega,v,2}$, $\hat{P}_{\omega,v}$, start to emerge in the entire z region, and gradually develop into similar appearances as those shown in Fig. 7(b) for the CS mode, except for the central peak structure of $\hat{S}_{\omega,v,1}$

This is the author's peer reviewed, accepted manuscript. However, the online version of record will be different from this version once it has been copyedited and typeset.

PLEASE CITE THIS ARTICLE AS DOI: 10.1063/1.50083687

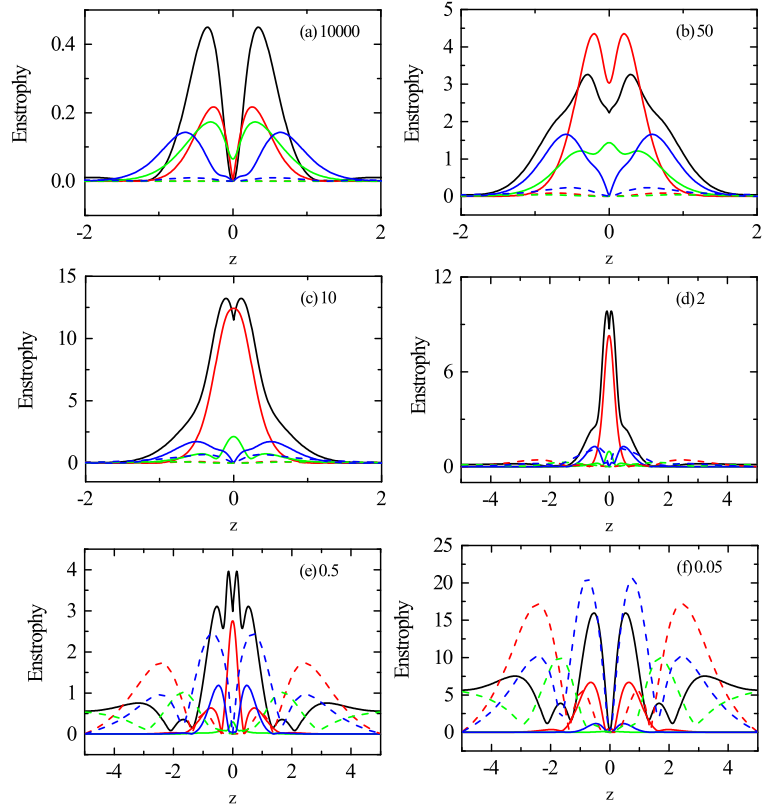


FIG. 9. The profiles of the absolute values of the enstrophy budget of the perturbations for the CS flow in the z direction at fixed $\chi = 0.06$, with decreasing ψ of: (a) 10000, (b) 50, (c) 10, (d) 2, (e) 0.5, and (f) 0.05. (—), (—), (—), (—), (---), (---), and (---) denote $D\hat{\omega}^2/Dt$, $\hat{S}_{\omega,u,1}$, $\hat{S}_{\omega,u,2}$, $\hat{P}_{\omega,u}$, $\hat{S}_{\omega,v,1}$, $\hat{S}_{\omega,v,2}$, and $\hat{P}_{\omega,v}$ respectively.

over $z \in [-1, 1]$ as the byproduct of the deformations of the OW mode inherited from the first stage. It is noted that the remaining central peak structure of $\hat{S}_{\omega,v,1}$ is still degenerating during the second stage. Nonetheless, both the features of the OW and CS modes coexist, accordingly the eigenfunction mode belongs to the ‘hybrid’ mode. In the third stage, the central peak structure of $\hat{S}_{\omega,v,1}$ signifying the OW mode completely decays into negligence

This is the author's peer reviewed, accepted manuscript. However, the online version of record will be different from this version once it has been copyedited and typeset.

PLEASE CITE THIS ARTICLE AS DOI: 10.1063/1.50083687

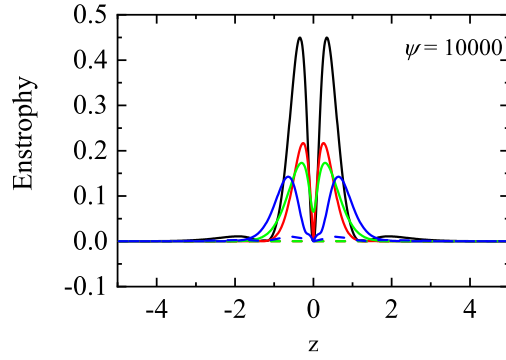


FIG. 10. The evolution of the profiles of the absolute values of the enstrophy budget of the perturbations for the CS flow in the z direction with fixed $\chi = 0.06$ and varying ψ values over $\psi = 0.001 \sim 10000$. (—), (—), (—), (—), (---), (---), and (---) denote $D\hat{\omega}^2/Dt$, $\hat{S}_{\omega,u,1}$, $\hat{S}_{\omega,u,2}$, $\hat{P}_{\omega,u}$, $\hat{S}_{\omega,v,1}$, $\hat{S}_{\omega,v,2}$, and $\hat{P}_{\omega,v}$ respectively. (Multimedia view)

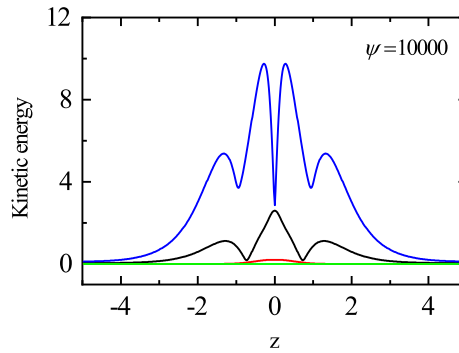


FIG. 11. The evolution of the profiles of the absolute values of the kinetic energy budget of the perturbations for the CS flow in the z direction with fixed $\chi = 0.06$ and varying ψ values over $\psi = 0.001 \sim 10000$. (—), (—), (—), (—), (---), (---), and (---) denote $D\hat{\omega}^2/Dt$, $\hat{S}_{\omega,u,1}$, $\hat{S}_{\omega,u,2}$, $\hat{P}_{\omega,u}$, $\hat{S}_{\omega,v,1}$, $\hat{S}_{\omega,v,2}$, and $\hat{P}_{\omega,v}$ respectively. (Multimedia view)

at $\psi = 0.05$ as shown in Fig. 9(f), indicating that the hybrid mode has transitioned into the CS mode, which continues to be the dominant mode as ψ decreases from 0.05. For the eigenfunctions of the kinetic energy budget, as shown in Fig. 11 (Multimedia view) where the profiles of the absolute values of the kinetic energy budget of the perturbations for the CS flow in the z direction with fixed $\chi = 0.06$ and varying ψ values over $\psi = 0.001 \sim 10000$ are presented to demonstrate the entire transitions, similar second and third transitional stages are observed, in spite of their different appearances.

The first transitional stage described above is closely related to how the enhanced cross shear deteriorates the basic eigenfunctions of the OW mode. To demonstrate this, Fig. 12 shows the eigenfunctions of \hat{p} at fixed $\chi = 0.06$ with ψ decreasing from 10000 to 2, the range corresponding to the first transitional stage of the enstrophy budget observed in Fig. 9(a)-(d). As ψ decreases, the three-peak structure of \hat{p} decays significantly, with the two side peaks, 'L' and 'R' peaks, vanished at $\psi = 50$, so that only the single 'C' peak of \hat{p} remains, leaving the overall \hat{p} structures to have the same appearance as those of the CS mode at $\psi = 1$ as shown in Fig. 9(b). Only after the establishment of its central peak structure at $\psi = 50$, the eigenfunction of \hat{p} can further increase its magnitude with little variation of its shape, which corresponds to the second transitional stage.

Similar to the establishment of the single-peak structure of \hat{p} as shown in Fig. 12(a), for other basic eigenfunctions not shown here, as ψ decreases their original eigenfunctions associated with the OW mode always experience a series of deformations to firstly transform into the appearances of the eigenfunctions associated with CS mode, which corresponds to the first transitional stage. Only when their appearances become similar to those associated with the CS mode, these basic eigenfunctions stop deforming their shapes to increase their magnitudes only, *e.g.*, the growth of the single-peak structure of \hat{p} as shown in Fig. 12(b). This means that the developments of the OW and the CS mode always compete with each other. As ψ decreases, the enhanced cross shear must first deteriorates the OW mode to a critical degree, which is in favor of the CS mode, then the cross shear is able to help the CS mode to grow further.

The concept of the competition between the OW mode and the CS mode can also explain the transition of the enstrophy as shown in Fig. 9. After a series of deformations, the profile of $\hat{S}_{\omega,u,1}$ signifying the OW mode is shrunk within the confined central region of $z \in [-1, 1]$. The reason for such a degeneration of $\hat{S}_{\omega,u,1}$ is because the eigenfunctions associated with

CS mode, *i.e.*, $\hat{S}_{\omega,v,1}$ and $\hat{P}_{\omega,v}$ in Fig. 7(b), inherently compete with the OW mode whose original $\hat{S}_{\omega,u,1}$ at $\psi < 2$ occupies the same central region. To ensure the development of the CS mode, the enhanced cross shear must first confine the original $\hat{S}_{\omega,u,1}$ structure associated with the OW mode into a limited central region, that is, the deformations of $\hat{S}_{\omega,u,1}$ shown in Fig. 9(a)-(d). Only after the confinement of the OW mode is achieved, the eigenfunctions associated with the CS mode can grow, *e.g.*, the 'L' and 'R' peaks of $\hat{S}_{\omega,v,1}$ and $\hat{P}_{\omega,v}$ as shown in Fig. 9(e)-(f).

Strictly speaking, there is no hybrid mode for \hat{p} as demonstrated by Fig. 12, as the profile of \hat{p} has already achieved its transformation at $\psi = 50$. Similar transitional behavior is found for all basic eigenfunctions, *i.e.*, \hat{u} , \hat{v} , \hat{w} , $\hat{\omega}_x$, $\hat{\omega}_y$, and $\hat{\omega}_z$. The reason for the hybrid mode of the eigenfunctions of the enstrophy budget is because the critical ψ , which indicates the transition from the OW mode to the CS mode being attained, is different for different basic eigenfunctions. For example, even when \hat{p} is transformed into the appearances of the CS mode at $\psi = 50$, $\hat{\omega}_x$ and $\hat{\omega}_z$ still possess the features of the OW mode, which is why the overall eigenfunctions of the enstrophy budget at $\psi = 50$ as shown in Fig. 9(b) still belong to the OW mode. Likewise, the hybrid mode shown in Fig. 9(e)-(f) is also attributed to the unfinished transition of some basic eigenfunctions, *e.g.*, $\hat{\omega}_x$, $\hat{\omega}_z$ and their product $\hat{\omega}_x\hat{\omega}_z$ that determine the remaining central peak of $\hat{S}_{\omega,u,1}$.

Based on Fig. 9, the two critical ψ values, $\psi_{cr,ow} = 2$ and $\psi_{cr,cs} = 0.05$ signifying the commencement of the dominance of the CS mode and the complete decay of the OW mode can serve as the boundaries of the hybrid mode, where the subscript 'ow' and 'cs' indicate that the adjacent eigenfunction modes to the hybrid mode are the OW mode and the CS mode, respectively. Likewise, for other χ values along the path, similar transitions as exhibited for $\chi = 0.06$ shown in Fig. 9 are also found, but with different $\psi_{cr,ow}$ and $\psi_{cr,cs}$ at different χ . After collecting all results of $\psi_{cr,ow}$ and $\psi_{cr,cs}$ along the path, the map of the effective regions of the OW mode, the CS mode and the hybrid mode is obtained as shown in Fig. 13. It is found that the upper boundary of the hybrid mode region expands as χ is near the stability boundary, indicating that the deformation of the OW mode in terms of $\psi_{cr,ow}$ occurs at larger ψ values, followed by the emergence of the CS mode in terms of the peak structures of $\hat{S}_{\omega,v}$. The expansion of the lower boundary always occurs as long as χ increases along the path, suggesting that the residual influence of the OW mode, *i.e.*, the central peak structure of $\hat{S}_{\omega,u,1}$ exhibited in Fig. 9(e), can survive at smaller ψ values.

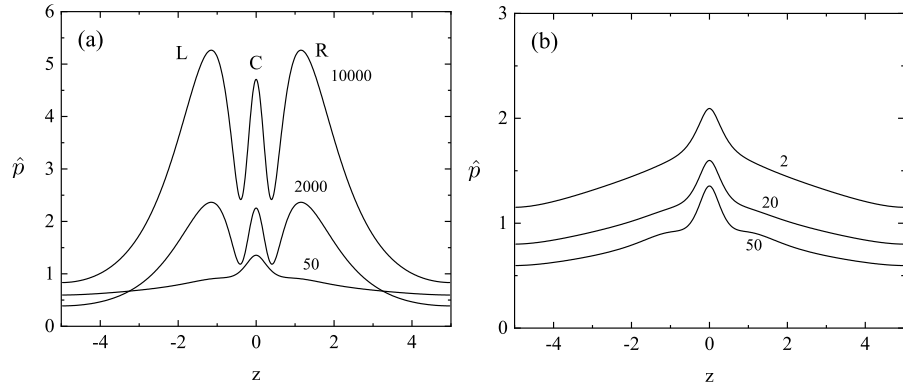


FIG. 12. The profiles of the absolute values of \hat{p} in the z direction at $\chi = 0.06$ with different ψ values (labeled by the numbers): (a) $\psi = 50, 2000,$ and 10000 , (b) $\psi = 2, 20,$ and 50 , respectively.

V. DISCUSSION AND CONCLUSIONS

This paper focuses on the hydrodynamics of the inviscid, free sheared and homogeneous CS flow, with the unstable primary velocity component $U = \tanh(z)$ and the stable orthogonal velocity component $V = \xi z^3$. By applying the normal mode, a combined multiplier factor $\chi = (\beta/\alpha) \xi$, which incorporates the influences of the ratio of the orthogonal wavenumber and the primary wavenumber β/α and the cross shear ratio ξ , is introduced in the linearized perturbation equations. By solving the eigenvalue problems pertaining to the perturbation equations, the map of the unstable region bounded by the unique stability boundary is obtained, indicating that the stable $V = \xi z^3$ indeed stabilizes the entire CS flow.

By solving the associated eigenfunction problems, two distinctive modes, the OW mode and the CS mode, are found when β/α or ξ absolutely dominate over each other. Because of the twisted features inherently existed in the CS flow, the eigenfunctions of both the OW mode and the CS mode involve the distinctively different structures compared to those associated with the PS flow. For the OW mode, the dominant β/α reduces the length scales of the perturbed flow structures and splits them into multiple scattered regions, yet the stabilization is still determined by the remaining but limited influences of the cross

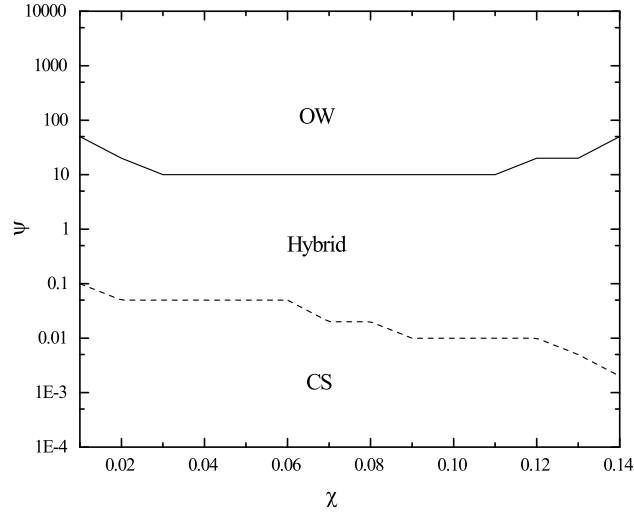


FIG. 13. The regions of the eigenfunction modes in the (χ, ψ) map along the path for the enstrophy budget.

shear on vortex deformation. For the CS mode, the dominance of ξ directly contributes to the absolute domination of \hat{v} , $\hat{\omega}_y$ and $\hat{\omega}_z$ over other basic eigenfunctions in the orthogonal direction, consequently introducing the strong stabilization effects that extend over the entire z region. Yet the remaining but compromised influences of the primary shear on vortex deformation sustain the destabilization in the limited central region.

The transitions among the OW mode, the CS mode and their hybrid mode are examined in terms of the relative ratio $\psi = (\beta/\alpha)/\xi$. It is found that the OW mode and the CS mode inherently compete with each other, so that the enhanced cross shear in terms of decreased ψ must first deteriorate the eigenfunctions of the OW mode before it supports the growth of the CS mode. In addition, the critical ψ values indicating the completion of the transition from the OW mode to the CS mode, are different for different basic eigenfunctions, thereby directly resulting in the hybrid mode of the kinetic energy and enstrophy budgets. Based on the critical $\psi_{cr,ow}$ and $\psi_{cr,cs}$ values that distinguish the hybrid mode from the OW mode

and the CS mode, respectively, the map of the three eigenfunction modes in terms of ψ and χ is obtained, in which the region of the hybrid mode expands near the stability boundaries, due to the enhanced role of the cross shear along the path, which not only depends on ψ but also on χ .

Though the role of the spanwise velocity on the stabilization of the non-parallel flow was confirmed in previous studies, the evidences are rather implicit. For instance, in Wojcik & Buchholz³¹, the stabilization of the spanwise velocity is only modeled as a source term in the vorticity budget without considering its dependence on the spatial coordinates. By directly imposing a stable spanwise/orthogonal velocity to the non-parallel flow, the present study shows that the stable spanwise velocity and the associated cross shear is not just an implicit, but a necessary condition for stabilization. In the perturbation equations, ξ must be non-zero to keep the term $i - \frac{\tilde{\alpha}\tilde{\beta}}{\alpha}(V\nabla_s^2 - V_{zz})$ of the non-parallelism. In addition, the stability boundary is uniquely created by the stable V , because if V is unstable, the CS flow would be unstable as well. In addition, the stabilization of V and the cross shear is elaborated by the vortex deformations that are only available for the CS flow. The role of the vortex deformation is also confirmed by a series of previous investigations on stabilization of the non-parallel flow^{19,31,33}, nevertheless, the present study shows the further dynamical complexity, that is, the OW and CS modes as well as their transition to each other. Though the two modes involve distinctively different mechanisms, essentially it is still the cross shear which achieves the stabilization.

Some further implications from current linear temporal analysis are worthy of attention. First, as the necessary role of the cross shear is confirmed based on Fig. 2, is there a universal critical ξ_{cr} value analogous to the critical Richardson number $Ri_{cr} = 0.25$ for different stabilized CS flows with $V = \xi z^3$, or other stable V flows? Second, for a viscous flow, many eliminated terms in the kinetic energy and the enstrophy budgets related to the viscosity appear, which will further complicate the mechanisms that form the flow structures. Third, as the stabilization from the stable orthogonal velocity $V = \xi z^3$ and the associated cross shear is demonstrated, in the flow control is it possible to design certain methods directly based on stable V and cross shear? Although our investigation in this paper is limited to unstratified, inviscid and homogeneous CS flow, the concept that the overall stabilization of the flow may be significantly improved by imposing a stable orthogonal base flow, can possibly provide some suggestive implications for those engineering applications

that desire to suppress the turbulence. For instance, though introducing a stable spanwise velocity such as $V = \xi z^3$ to a global domain may be technically difficult, locally it is possible to impose and maintain such a stable spanwise velocity profile and the cross shear with satisfactory accuracy, via a sequence of synthetic (fluidic) jet actuators with proper vertical arrangements, such as the synthetic jet actuators applied in the unmanned air vehicles²¹. At low velocity, the arrangement of plasma actuators is also a potential way to induce the stable velocity, similar to its application in the flow control of the swept wing boundary layers⁴⁶. Perhaps, the current applications of these actuators in the separation or transition control of boundary flows more or less involve the local stabilization via the twisted vortex structures as suggested by Hwang *et al.*¹⁹ and Guercio *et al.*³³. With a more specific stable cross shear applied, the actuators can possibly be more efficient to achieve the local stabilization. In reality, the intensity of the imposed stable cross shear may be limited by the power of the actuators. Nevertheless, the overall non-parallel flow can still be stabilized, because, as suggested by the present study, it is both the misaligned base flow and the three-dimensional perturbations together to determine the stabilization, which is represented by the combined parameter $\chi = (\beta/\alpha)\xi$ governing the map of the stability as shown in Fig. 2(b). In other words, the existence of the stable cross shear ensures that the overall hydrodynamics of the non-parallel flow develops towards the stabilization, not the destabilization, thus the existence of the stable cross shear is more important than its magnitude. As χ is determined together by ξ and (β/α) , even if the intensity of the stable cross shear is limited, it can still increase the frequency/wavenumber of the imposed perturbations to amplify the overall stabilization. At last, we also believe that with more advanced linear temporal-spatial analysis and non-linear analysis, some more concepts will be further developed in the future.

SUPPLEMENTARY MATERIAL

See the Supplementary Material for the detailed derivation of the linearized perturbation equations.

DECLARATIONS OF COMPETING INTEREST

The authors declare that they have no conflicts of interest to disclose.

DATA AVAILABILITY

The data that support the findings of this study are available from the corresponding author upon reasonable request.

REFERENCES

- ¹M. O. Kramer, "Boundary layer stabilization by distributed damping," *Naval Engrs. J.* **74**, 341–348 (1962).
- ²D. M. Bushnell, J. N. Hefner, and R. L. Ash, "Effect of compliant wall motion on turbulent boundary layers," *Phys. Fluids* **20**(10), S31–S48 (1977).
- ³M. Gad-el-Hak, *Flow Control: Passive, Active, and Reactive Flow Management* (Cambridge University Press, New York, 2000).
- ⁴M. Malik, M. Skote, and R. Bouffanais, "Growth mechanisms of perturbations in boundary layers over a compliant wall," *Phys. Rev. Fluids* **3**(1), 013903 (2018).
- ⁵P. T. Nagy and G. Paal, "Stabilization of the boundary layer by streamwise control," *Phys. Fluids* **31**, 124107 (2019).
- ⁶K. Fukagata, S. Kern, P. Chatelain, P. Koumoutsakos, and N. Kasagi, "Evolutionary optimization of an anisotropic compliant surface for turbulent friction drag reduction," *J. Turbul.* **9**, N35 (2008).
- ⁷Q.-J. Xia, W.-X. Huang, and C.-X. Xu, "Direct numerical simulation of turbulent boundary layer over a compliant wall," *J. Fluids Struct.* **71**, 126–142 (2017).
- ⁸C. Zhang, J. Wang, W. Blake, and J. Katz, "Deformation of a compliant wall in a turbulent channel flow," *J. Fluid Mech.* **823**, 345–390 (2017).
- ⁹T. I. Jozsa, E. Balaras, M. Kashtalyan, A. G. L. Borthwick, and I. M. Viola, "Active and passive in-plane wall fluctuations in turbulent channel flows," *J. Fluid Mech.* **866**, 689–720 (2019).
- ¹⁰M. Sarioglu, "Control of flow around a square cylinder at incidence by using a splitter plate," *Flow Meas. Instrum.* **53**(B), 221–229 (2017).
- ¹¹H.-C. Lim and S.-J. Lee, "Flow control of circular cylinders with longitudinal grooved

This is the author's peer reviewed, accepted manuscript. However, the online version of record will be different from this version once it has been copyedited and typeset.

PLEASE CITE THIS ARTICLE AS DOI: 10.1063/1.50083687

- surfaces," *AIAA J.*, **40**(10), 2027–2036 (2002).
- ¹²I. M. Gorban and O. V. Khomenko, "Active near-wall flow control via a cross groove with suction," In *Continuous and Distributed Systems II. Studies in Systems, Decision and Control, vol 30*, V. Sadvnichiy and M. Zgurovsky (eds) (Springer, 2015).
- ¹³S.-J. Lee, H.-C. Lim, M. Han, and S. S. Lee, "Flow control of circular cylinder with a V-grooved micro-riblet film," *Fluid Dyn. Res.*, **37**, 246–266 (2005).
- ¹⁴C. Canpolat and B. Sahin, "Influence of single rectangular groove on the flow past a circular cylinder," *Int. J. Heat Fluid Flow*, **64**, 79–88 (2017).
- ¹⁵J. C. Schulmeister, J. M. Dahl, G. D. Weymouth, and M. S. Triantafyllou, "Flow control with rotating cylinder," *J. Fluid Mech.* **825**, 743–763 (2017).
- ¹⁶X. Shi, S. Xu, L. Ding, and D. Huang, "Passive flow control of a stalled airfoil using an oscillating micro-cylinder," *Comp. Fluids* **178**, 152–165 (2019).
- ¹⁷H. Choi, W.-P. Jeon, and J. Kim, "Control of flow over a bluff body," *Annu. Rev. Fluid Mech.* **40**, 113–139 (2008).
- ¹⁸D. Serson, J. R. Meneghini, and S. J. Sherwin, "Direct numerical simulations of the flow around wings with spanwise waviness at a very low Reynolds number," *Comp. Fluids* **146**, 117–124 (2017).
- ¹⁹Y. Hwang, J. Kim, and H. Choi, "Stabilization of absolute instability in spanwise wavy two-dimensional wakes," *J. Fluid Mech.* **727**, 346–378 (2013).
- ²⁰C. M. Crispo, C. S. Greco, F. Avallone, and G. Cardone, "On the flow organization of a chevron synthetic jet," *Exp. Therm. Fluid Sci.* **82**, 136–146 (2017).
- ²¹D. Greenblatt and D. R. Williams, "Flow control for unmanned air vehicles," *Annu. Rev. Fluid Mech.* **54** (2022).
- ²²M. Kelso and J. Smits, "Horseshoe vortex systems resulting from the interaction between a laminar boundary layer and a transverse jet," *Phys. Fluids* **7**(1), 153–158 (1995).
- ²³M. Krishnan, "The interaction of jets with crossflow," *Annu. Rev. Fluid Mech.* **45**, 379–407 (2013).
- ²⁴P. Atsavapranee and M. Gharib, "Structures in stratified plane mixing layers and the effects of cross-shear," *J. Fluid Mech.* **342**, 53–86 (1997).
- ²⁵J. Lin, Z. Yu, and X. Shao, "Numerical research on coherent structures in a mixing layer with cross-shear," *J. Fluids Struct.* **16**(4), 487–495 (2002).
- ²⁶K. Deguchi, "Inviscid instability of a unidirectional flow sheared in two transverse direc-

This is the author's peer reviewed, accepted manuscript. However, the online version of record will be different from this version once it has been copyedited and typeset.

PLEASE CITE THIS ARTICLE AS DOI: 10.1063/5.0083687

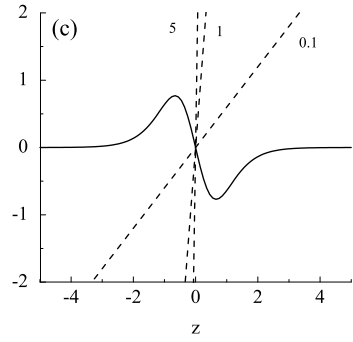
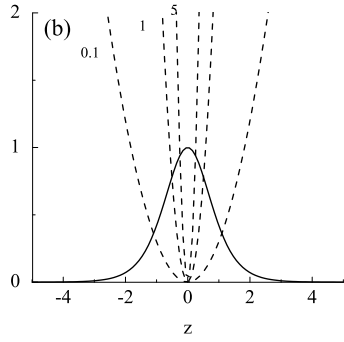
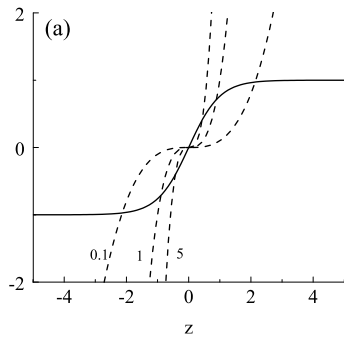
- tions," J. Fluid Mech. **874**, 979–994 (2019).
- ²⁷A. Peplinski, P. Schlatter, and D. Henningson, "Global stability and optimal perturbation for a jet in cross-flow," Euro. J. Mech. B/Fluids. **49**, 438–447 (2015).
- ²⁸M. Regan and K. Mahesh, "Global linear stability analysis of jets in cross-flow," J. Fluid Mech. **828**, 812–836 (2017).
- ²⁹G. Chauvat, A. Peplinski, D. Henningson, and A. Hanifi, "Global linear analysis of a jet in cross-flow at low velocity ratios," J. Fluid Mech. **889**, A12 (2020).
- ³⁰Y. Xiao and W. Lin, "Linear temporal stability analysis on non-parallel free cross sheared flow with a primary hyperbolic velocity and an orthogonal Bickley jet velocity," Phys. Fluids **33**, 124101 (2021).
- ³¹C. J. Wojcik and J. H. Buchholz, "Vorticity transport in the leading-edge vortex on a rotating blade," J. Fluid Mech. **743**, 249–261 (2014).
- ³²T. Jardin, "Coriolis effect and the attachment of the leading edge vortex," J. Fluid Mech. **820**, 312–340 (2017).
- ³³G. D. Guercio, C. Cossu, and G. Pujals, "Stabilizing effect of optimally amplified streaks in parallel wakes," J. Fluid Mech. **739**, 37–56 (2014).
- ³⁴R. Fjørtoft, "Application of integral theorems in deriving criteria of stability for laminar flows and for the baroclinic circular vortex," Geofys. Publ. **17**, 1–52 (1950).
- ³⁵P. G. Drazin and W. H. Reid, *Hydrodynamic Stability* (second edition) (Cambridge University Press, 2004).
- ³⁶F. T. M. Nieuwstadt, B. J. Boersma, and J. Westerweel, *Turbulence: Introduction to Theory and Applications of Turbulent Flows* (Springer, 2016).
- ³⁷P. J. Schmid and D. S. Henningson, *Stability and Transition in Shear Flows* (Springer, 2000).
- ³⁸H. B. Squire, "On the stability of three-dimensional disturbances of viscous flow between parallel walls," Proc. Roy. Soc. London Ser. A. **142**, 621–628 (1933).
- ³⁹C. B. Moler and G. W. Stewart, "An algorithm for generalized matrix eigenvalue problems," SIAM J. Numer. Anal. **10**, 241–256 (1973).
- ⁴⁰Z. Liu, S. A. Thorpe, and W. D. Smyth, "Instability and hydraulics of turbulent stratified shear flows," J. Fluid Mech. **695**, 235–256 (2012).
- ⁴¹W. D. Smyth, D. J. Moum, and J. D. Nash, "Narrowband, high-frequency oscillations at the equator. Part II: Properties of shear instabilities," J. Phys. Oceanogr. **41**, 412–428

This is the author's peer reviewed, accepted manuscript. However, the online version of record will be different from this version once it has been copyedited and typeset.

PLEASE CITE THIS ARTICLE AS DOI: 10.1063/1.50083687

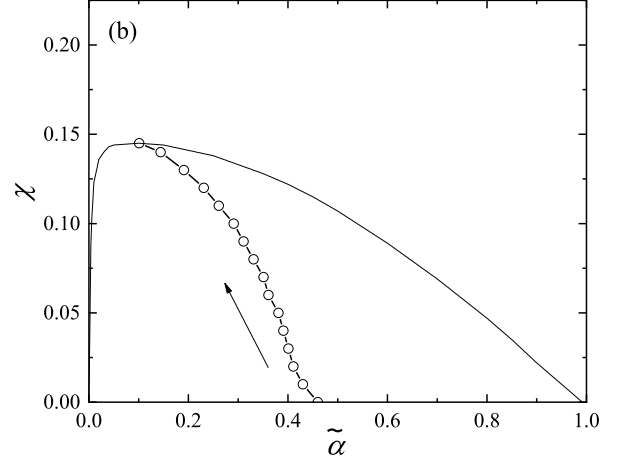
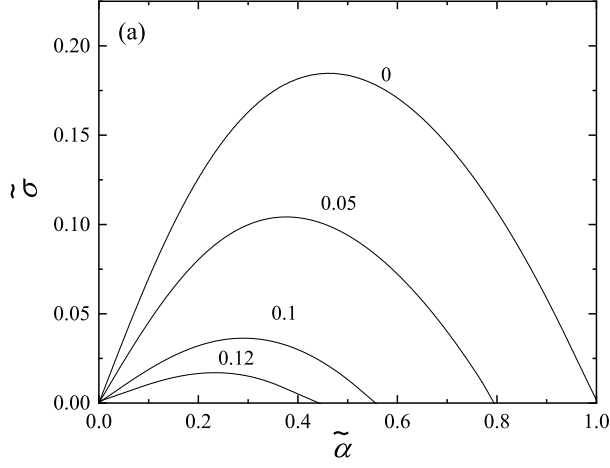
- (2011).
- ⁴²S. A. Thorpe, W. D. Smyth, and L. Li, “The effect of small viscosity and diffusivity on the marginal stability of stably stratified shear flows,” *J. Fluid Mech.* **731**, 461–476 (2013).
- ⁴³P. G. Drazin and L. N. Howard, “Hydrodynamic stability of parallel flow in inviscid fluid,” *Adv. Applied Mech.* **9**, 1–89 (1966).
- ⁴⁴P. Hazel, “Numerical studies of the stability of inviscid stratified shear flows,” *J. Fluid Mech.* **51**, 39–61 (1972).
- ⁴⁵W. D. Smyth and W. R. Peltier, “The transition between Kelvin-Helmholtz and Holmboe instability: an investigation of the overreflection hypothesis,” *J. Atmos. Sci.* **46**, 3698–3720 (1989).
- ⁴⁶J. Serpieri, “Cross-flow instability: flow diagnostics and control of swept wing boundary layers,” PhD thesis. Delft University of Technology (2018).

This is the author's peer reviewed, accepted manuscript. However, the online version of record will be different from this version once it has been copyedited and typeset.
 PLEASE CITE THIS ARTICLE AS DOI: 10.1063/5.0083687



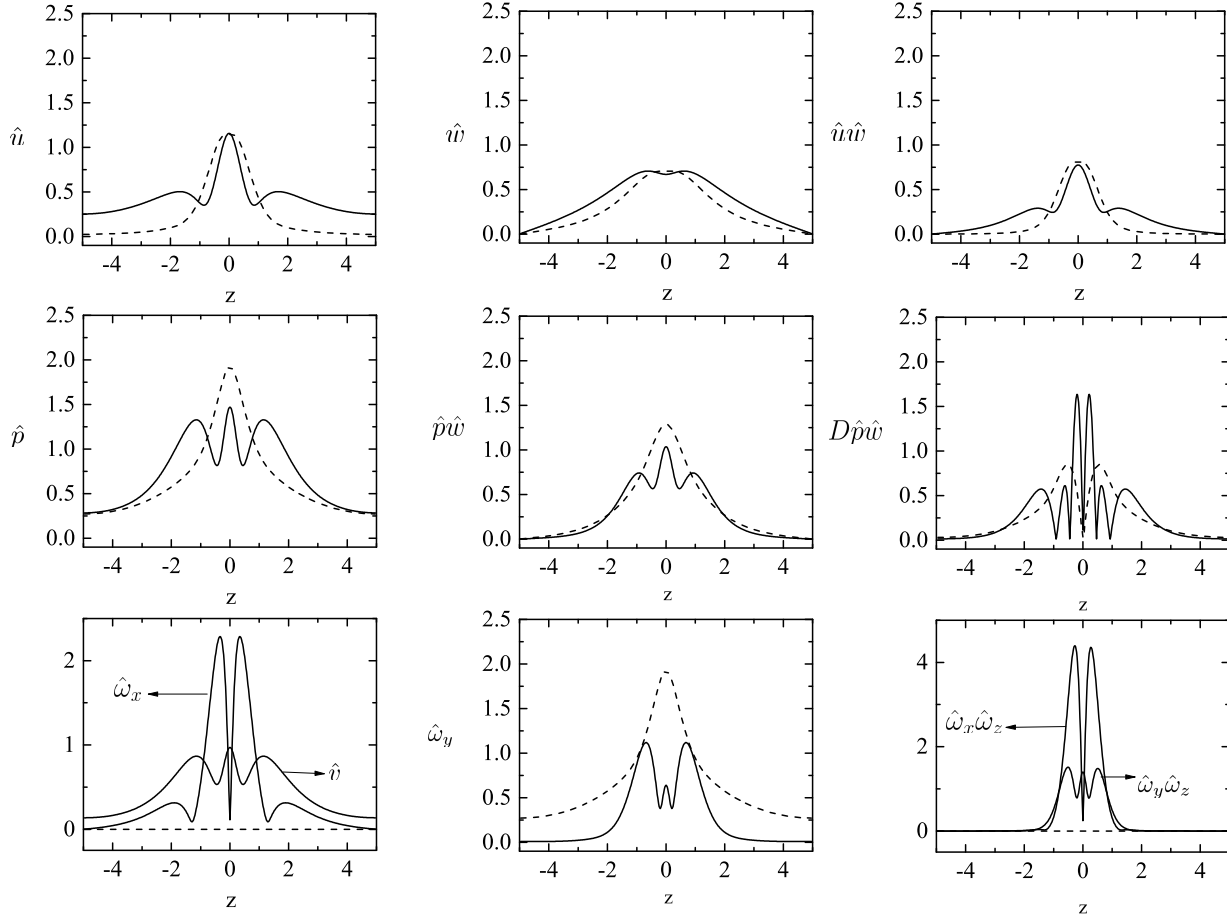
This is the author's peer reviewed, accepted manuscript. However, the online version of record will be different from this version once it has been copyedited and typeset.

PLEASE CITE THIS ARTICLE AS DOI: 10.1063/1.50083687



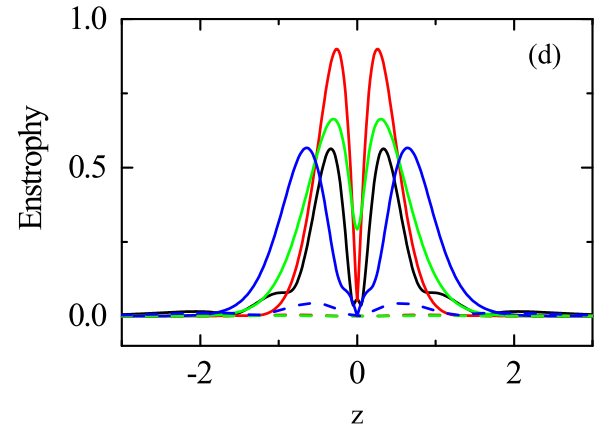
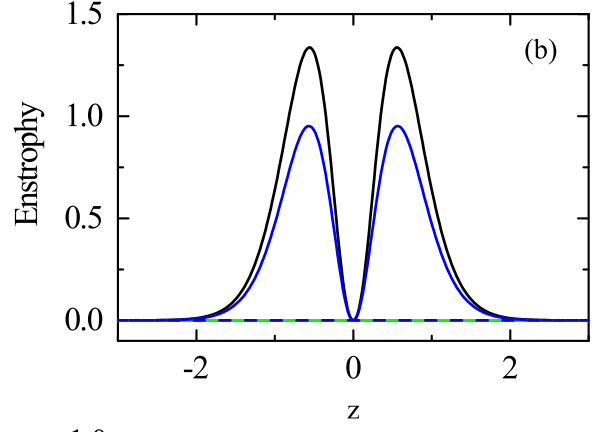
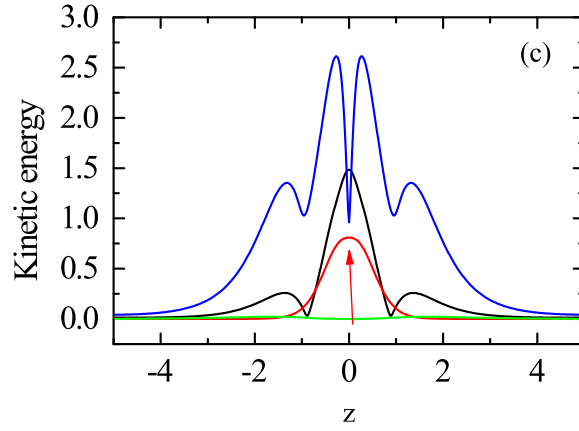
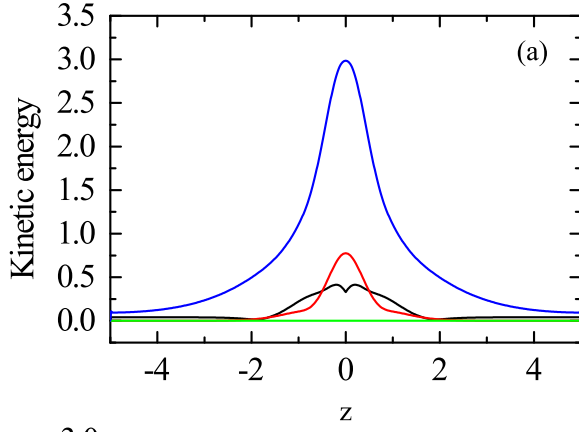
This is the author's peer reviewed, accepted manuscript. However, the online version of record will be different from this version once it has been copyedited and typeset.

PLEASE CITE THIS ARTICLE AS DOI: 10.1063/1.50083687

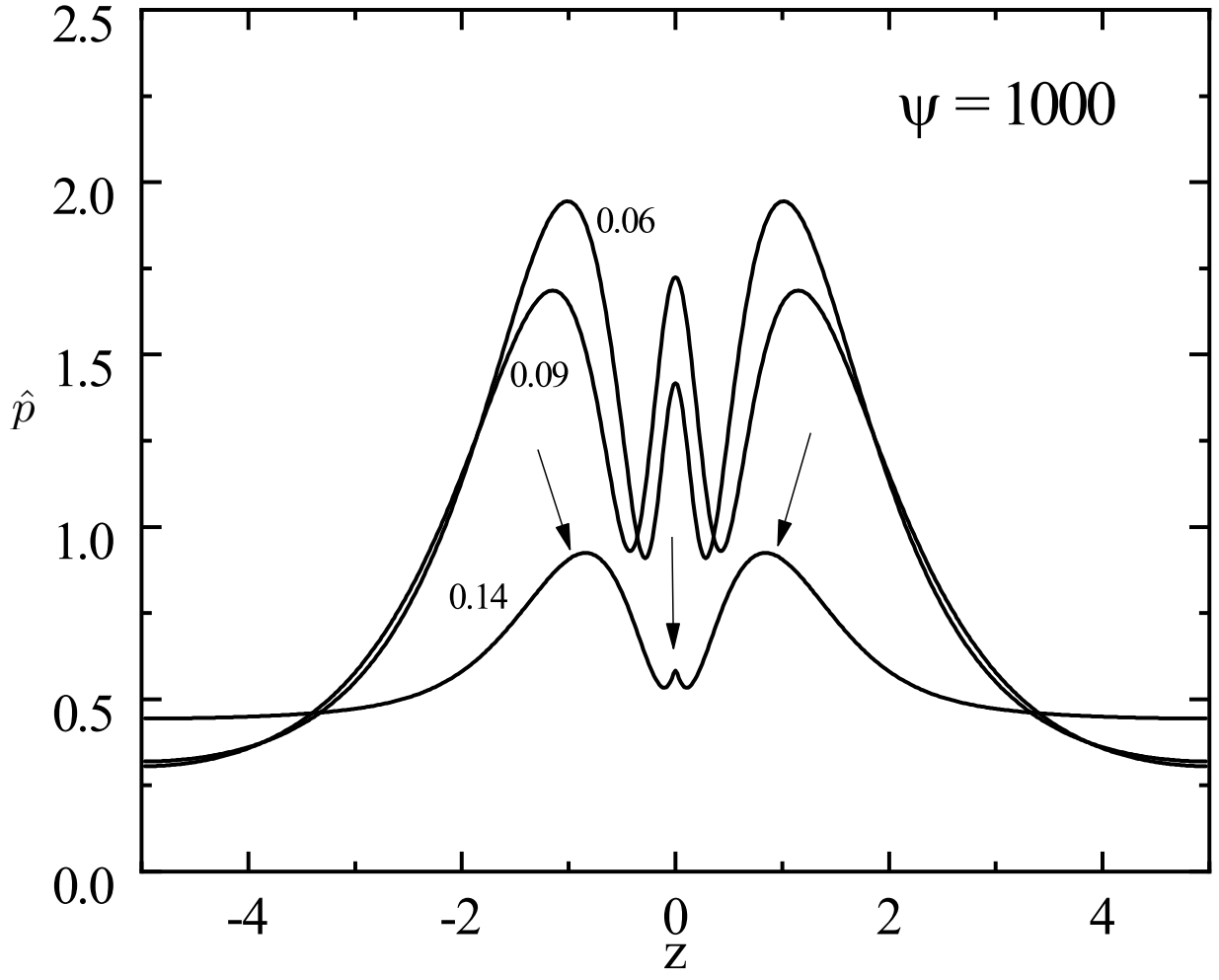


This is the author's peer reviewed, accepted manuscript. However, the online version of record will be different from this version once it has been copyedited and typeset.

PLEASE CITE THIS ARTICLE AS DOI: 10.1063/1.50083687

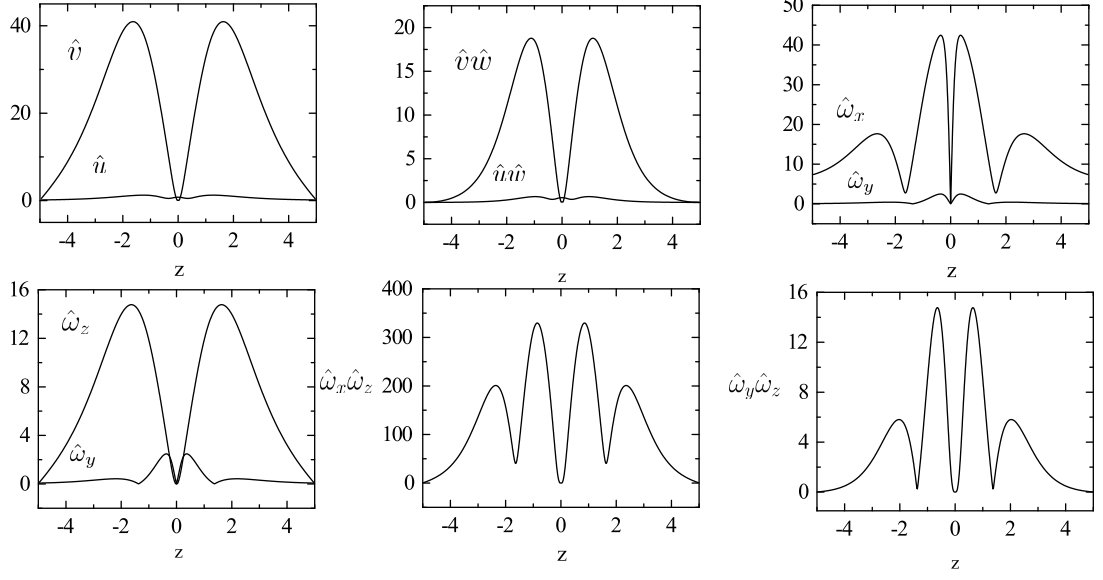


This is the author's peer reviewed, accepted manuscript. However, the online version of record will be different from this version once it has been copyedited and typeset.
 PLEASE CITE THIS ARTICLE AS DOI: 10.1063/1.50083687



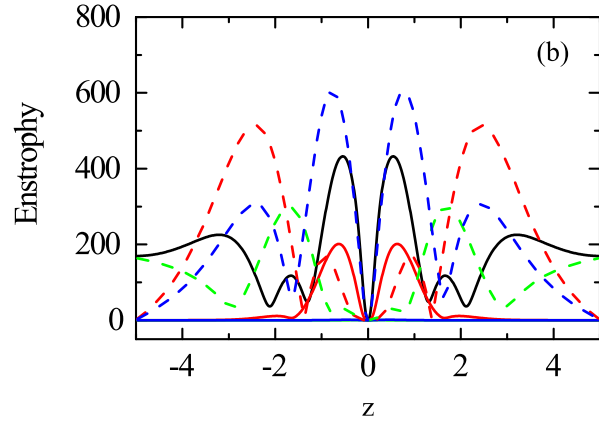
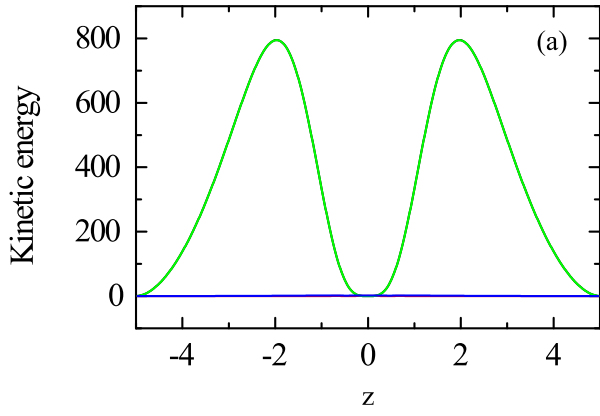
This is the author's peer reviewed, accepted manuscript. However, the online version of record will be different from this version once it has been copyedited and typeset.

PLEASE CITE THIS ARTICLE AS DOI: 10.1063/1.50083687



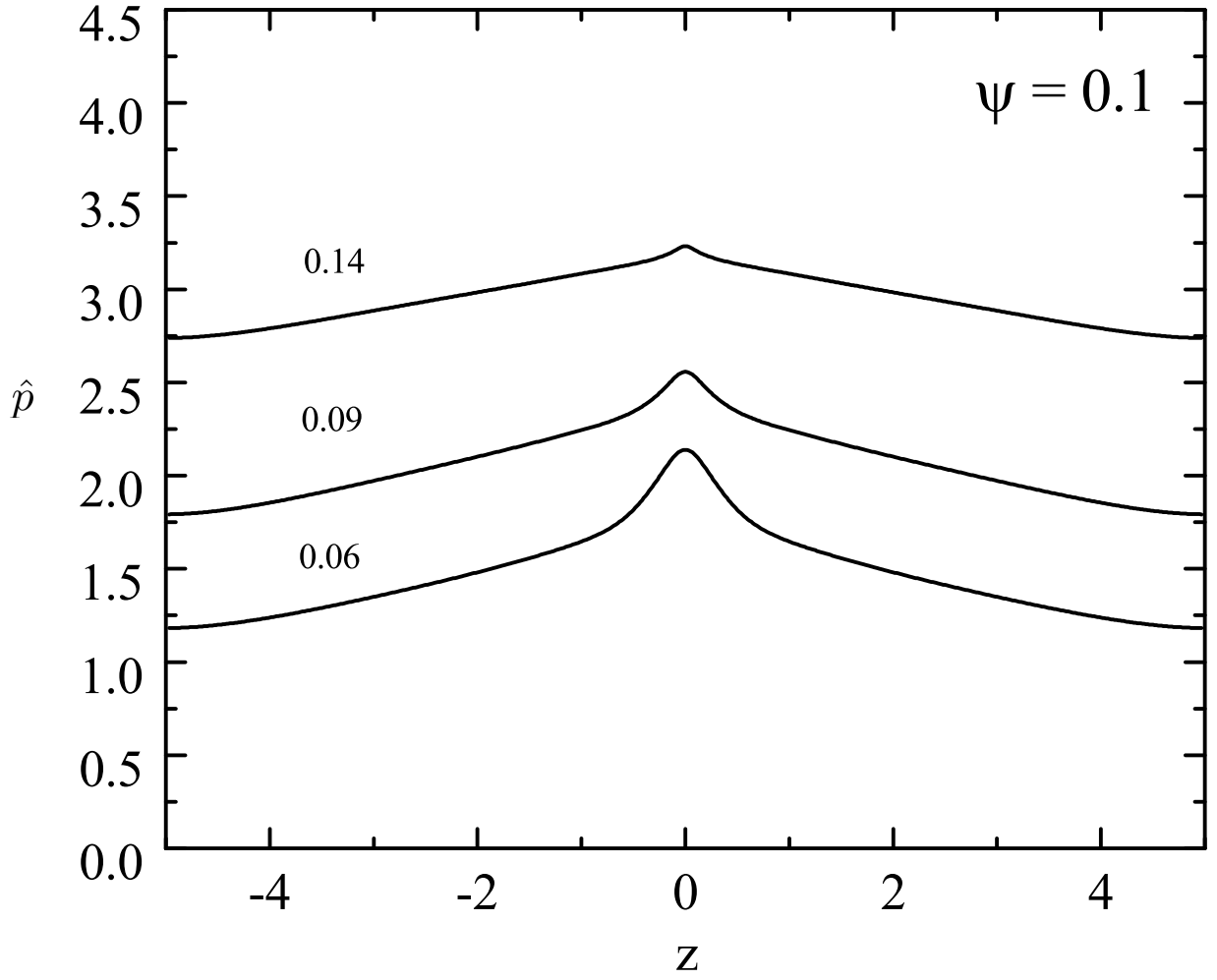
This is the author's peer reviewed, accepted manuscript. However, the online version of record will be different from this version once it has been copyedited and typeset.

PLEASE CITE THIS ARTICLE AS DOI: 10.1063/5.0083687



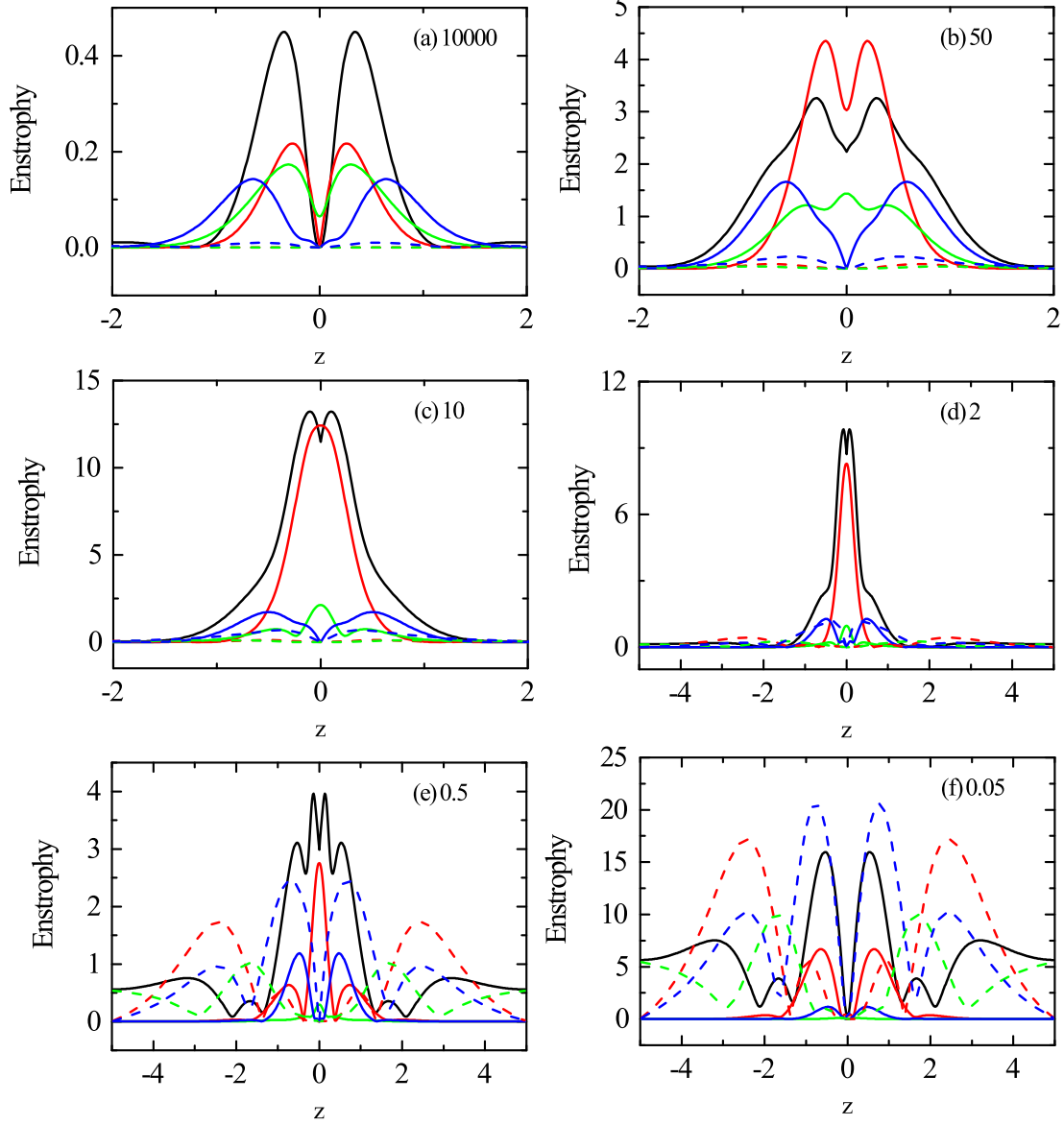
This is the author's peer reviewed, accepted manuscript. However, the online version of record will be different from this version once it has been copyedited and typeset.

PLEASE CITE THIS ARTICLE AS DOI: 10.1063/1.50083687



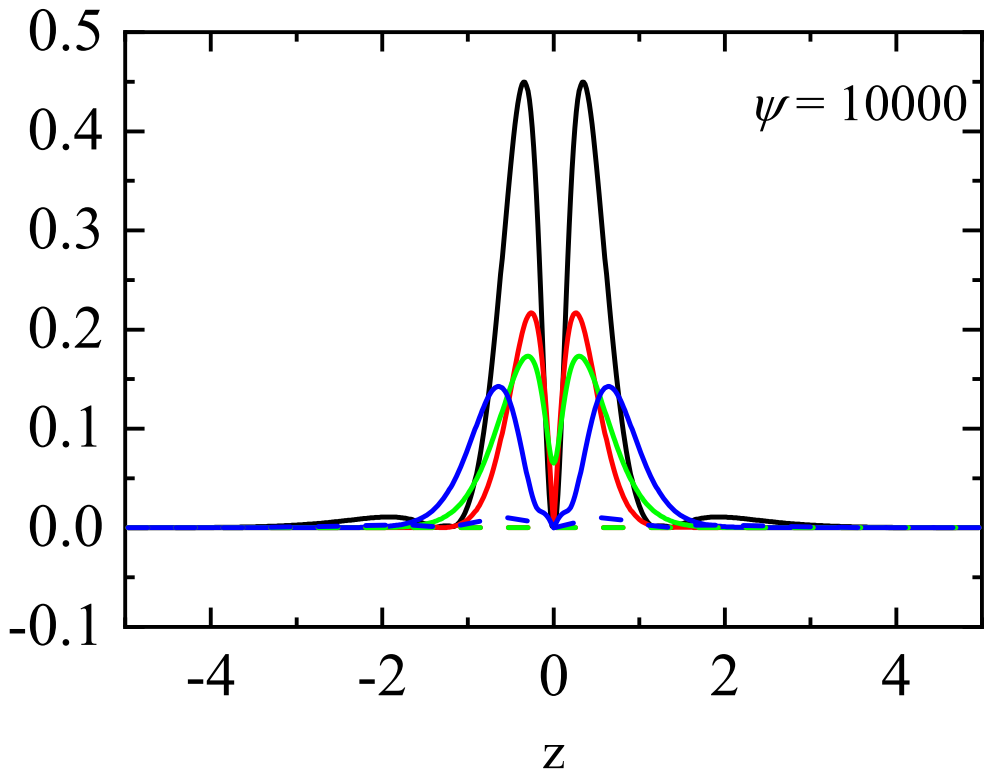
This is the author's peer reviewed, accepted manuscript. However, the online version of record will be different from this version once it has been copyedited and typeset.

PLEASE CITE THIS ARTICLE AS DOI: 10.1063/1.50083687

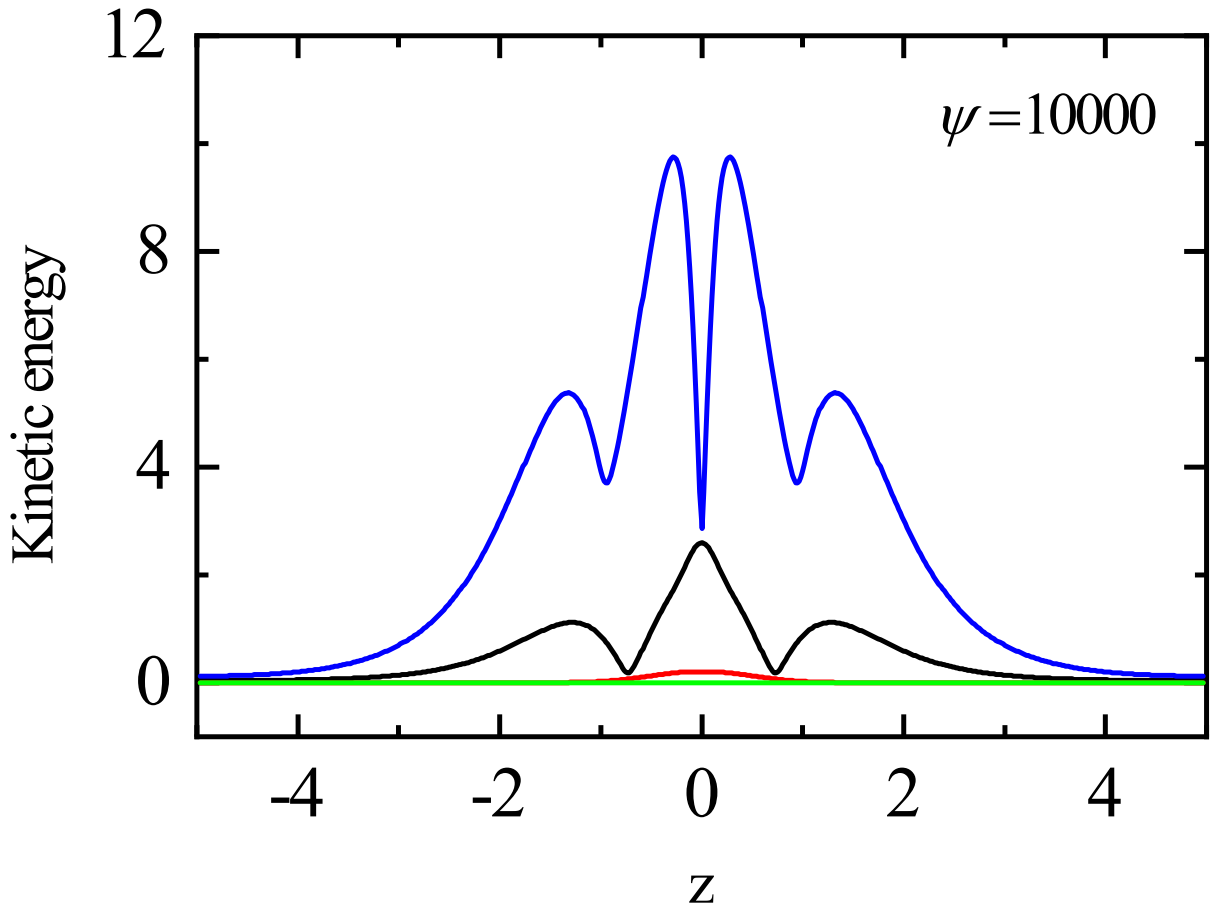


This is the author's peer reviewed, accepted manuscript. However, the online version of record will be different from this version once it has been copyedited and typeset.
 PLEASE CITE THIS ARTICLE AS DOI: 10.1063/1.50083687

Enstrophy

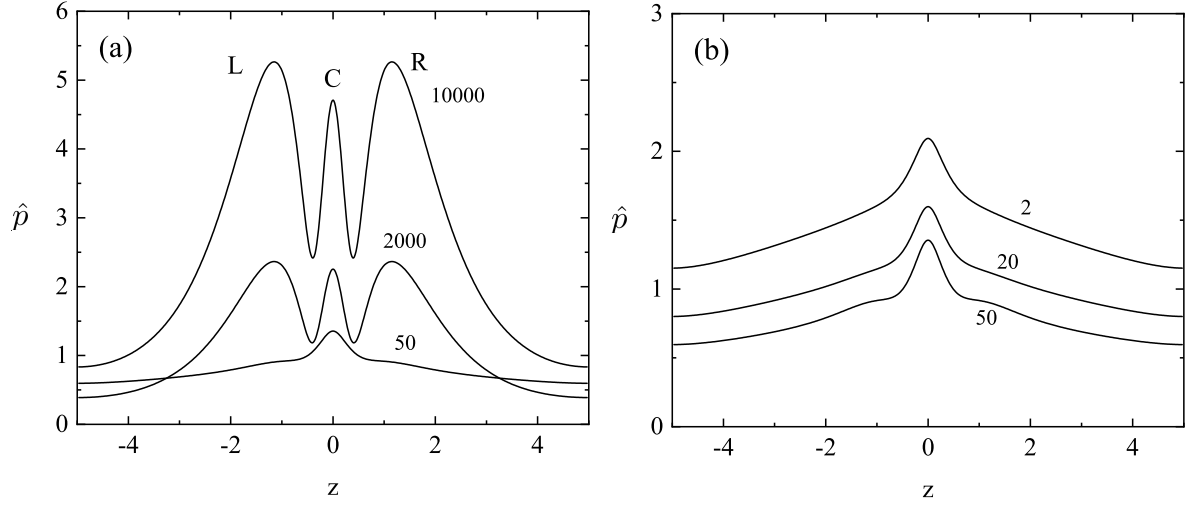


This is the author's peer reviewed, accepted manuscript. However, the online version of record will be different from this version once it has been copyedited and typeset.
 PLEASE CITE THIS ARTICLE AS DOI: 10.1063/1.50083687



This is the author's peer reviewed, accepted manuscript. However, the online version of record will be different from this version once it has been copyedited and typeset.

PLEASE CITE THIS ARTICLE AS DOI: 10.1063/5.0083687



This is the author's peer reviewed, accepted manuscript. However, the online version of record will be different from this version once it has been copyedited and typeset.

PLEASE CITE THIS ARTICLE AS DOI: 10.1063/1.50083687

